Earth Syst. Sci. Data, 14, 1063–1085, 2022
https://doi.org/10.5194/essd-14-1063-2022

Open Access Earth System Science Data

VODCA2GPP – a new, global, long-term (1988–2020) gross primary production dataset from microwave remote sensing

Benjamin Wild[1], Irene Teubner[1,2], Leander Moesinger[1], Ruxandra-Maria Zotta[1], Matthias Forkel[3], Robin van der Schalie[4], Stephen Sitch[5], and Wouter Dorigo[1]

[1]Department of Geodesy and Geoinformation, TU Wien, Wiedner Hauptstraße 8, 1040 Vienna, Austria
[2]Zentralanstalt für Meteorologie und Geodynamik (ZAMG), Hohe Warte 38, 1190 Vienna, Austria
[3]Environmental Remote Sensing Group, Institute of Photogrammetry and Remote Sensing, Technische Universität Dresden, Helmholtzstraße 10, 01069 Dresden, Germany
[4]VanderSat, Wilhelminastraat 43A, 2011 VK Haarlem, the Netherlands
[5]College of Life and Environmental Sciences, University of Exeter, Exeter, EX4 4QE, UK

Correspondence: Benjamin Wild (benjamin.wild@tuwien.ac.at)

Received: 22 June 2021 – Discussion started: 24 June 2021
Revised: 21 January 2022 – Accepted: 25 January 2022 – Published: 10 March 2022

Abstract. Long-term global monitoring of terrestrial gross primary production (GPP) is crucial for assessing ecosystem responses to global climate change. In recent decades, great advances have been made in estimating GPP and many global GPP datasets have been published. These datasets are based on observations from optical remote sensing, are upscaled from in situ measurements, or rely on process-based models. Although these approaches are well established within the scientific community, datasets nevertheless differ significantly.

Here, we introduce the new VODCA2GPP dataset, which utilizes microwave remote sensing estimates of vegetation optical depth (VOD) to estimate GPP at the global scale for the period 1988–2020. VODCA2GPP applies a previously developed carbon-sink-driven approach (Teubner et al., 2019, 2021) to estimate GPP from the Vegetation Optical Depth Climate Archive (Moesinger et al., 2020; Zotta et al., 2022), which merges VOD observations from multiple sensors into one long-running, coherent data record. VODCA2GPP was trained and evaluated against FLUXNET in situ observations of GPP and compared against largely independent state-of-the-art GPP datasets from the Moderate Resolution Imaging Spectroradiometer (MODIS), FLUXCOM, and the TRENDY-v7 process-based model ensemble.

The site-level evaluation with FLUXNET GPP indicates an overall robust performance of VODCA2GPP with only a small bias and good temporal agreement. The comparisons with MODIS, FLUXCOM, and TRENDY-v7 show that VODCA2GPP exhibits very similar spatial patterns across all biomes but with a consistent positive bias. In terms of temporal dynamics, a high agreement was found for regions outside the humid tropics, with median correlations around 0.75. Concerning anomalies from the long-term climatology, VODCA2GPP correlates well with MODIS and TRENDY-v7 (Pearson's r 0.53 and 0.61) but less well with FLUXCOM (Pearson's r 0.29). A trend analysis for the period 1988–2019 did not exhibit a significant trend in VODCA2GPP at the global scale but rather suggests regionally different long-term changes in GPP. For the shorter overlapping observation period (2003–2015) of VODCA2GPP, MODIS, and the TRENDY-v7 ensemble, significant increases in global GPP were found. VODCA2GPP can complement existing GPP products and is a valuable dataset for the assessment of large-scale and long-term changes in GPP for global vegetation and carbon cycle studies. The VODCA2GPP dataset is available at the TU Data Repository of TU Wien (https://doi.org/10.48436/1k7aj-bdz35, Wild et al., 2021).

1 Introduction

Gross primary production (GPP) describes vegetation's conversion of atmospheric CO_2 to carbohydrates through photosynthesis and is the largest CO_2 flux in the carbon cycle (Beer et al., 2010). GPP is also considered the primary driver of the terrestrial carbon sink responsible for the uptake of approximately 30 % of anthropogenic CO_2 emissions (Friedlingstein et al., 2020). GPP therefore plays a key role in mitigating the negative effects of anthropogenic emissions. Estimates of global mean annual GPP range from 112 (Anav et al., 2015) to 175 $Pg\,C\,yr^{-1}$ (Welp et al., 2011) but exhibit a high degree of interannual variability. GPP is strongly affected by increasing concentrations of CO_2 in the atmosphere and the associated global climate change (Haverd et al., 2020; Schimel et al., 2015; Cox et al., 2000). Quantifying GPP is essential to understand the effect of climate variability and changes in atmospheric CO_2 concentrations on the land carbon cycle (e.g. Baldocchi et al., 2016; Nemani et al., 2003).

Locally, GPP can be determined at in situ flux towers, which measure the net exchange of carbon dioxide by means of eddy covariances that are partitioned into GPP and ecosystem respiration fluxes (Baldocchi, 2003). FLUXNET (Pastorello et al., 2020) is the global network of flux towers covering all major biomes and provides the scientific community with harmonized and well-documented flux observations. FLUXNET stations, however, are sparsely and unevenly distributed, which complicates the derivation of GPP globally.

On the global scale, GPP is commonly estimated using optical remote sensing data in combination with (semi-)empirical or machine learning models (e.g. O'Sullivan et al., 2020; Jung et al., 2020; Gilabert et al., 2017; Alemohammad et al., 2017; Tramontana et al., 2016). Specifically, these models are based on light use efficiency (LUE) theory and/or statistical models that are applied to derive GPP based on optical remote sensing variables that are indicative of the vegetation's photosynthetic activity, such as the fraction of absorbed photosynthetically active radiation (fAPAR), the leaf area index (LAI), spectral vegetation indices, or sun-induced fluorescence (SIF). Datasets based on optical remote sensing have the advantage of being available globally with a high spatial resolution (usually on the order of 100 m to 1 km) and temporal resolution (e.g. every 8 d for the Moderate Resolution Imaging Spectroradiometer, MODIS). However, optical remote sensing is strongly affected by cloud cover, leading to data gaps and high uncertainties in regions with frequent cloud cover and high GPP such as tropical forests. Additionally, in very productive regions methods based on optical remote sensing tend to underestimate GPP because of the saturation of reflectance measurements in dense canopies (Turner et al., 2006).

Compared to optical remote sensing, vegetation optical depth (VOD) from microwave remote sensing is much less affected by weather conditions. VOD describes the vegetation's attenuation of radiation in the microwave domain, which is controlled by its water content, biomass, type, and density (Jackson and Schmugge, 1991; Vreugdenhil et al., 2016). Thus, VOD has been intensively used as a proxy for above-ground biomass (Li et al., 2021; Rodríguez-Fernández et al., 2018; Tian et al., 2016; Liu et al., 2015) and is becoming increasingly important for monitoring vegetation dynamics (e.g. Frappart et al., 2020; Piles et al., 2017).

Teubner et al. (2018, 2019, 2021) investigated how GPP can be estimated from VOD. First, they showed that GPP is significantly correlated with spatial patterns and temporal changes in VOD (Teubner et al., 2018). Based on this relationship, they developed a theoretical framework and a machine learning method using FLUXNET observations to predict GPP using VOD (Teubner et al., 2019). They showed that GPP can be adequately estimated for most regions of the world with an overall tendency towards moderate overestimation and good temporal agreement with existing GPP products, especially for temperate regions. Recently, Teubner et al. (2021) improved this method by adding air temperature into their model to account for the temperature dependence of plant respiration (Atkin and Tjoelker, 2003) and found that this significantly improved the temporal agreement with reference GPP data.

However, until recently, long-term analysis of GPP from VOD was complicated due to relatively short observation periods of individual passive microwave remote sensing sensors (Moesinger et al., 2020). Moesinger et al. (2020) overcame this issue by merging single-frequency VOD from various sensors into the long-term Vegetation Optical Depth Climate Archive (VODCA), which comprises VOD observations of more than 20 years for the X- and C-band and more than 30 years for the Ku-band. A new version of VODCA (Zotta et al., 2022) not only combines single sensors from identical frequencies but also merges observations from different bands (X, C, and Ku) into a single long-running, multi-frequency VOD climate archive with improved quality.

Here, our objective is to generate, evaluate, and describe a novel long-term GPP dataset by applying the approach of Teubner et al. (2019, 2021) to the VODCA dataset. This microwave-based GPP dataset can likely complement existing datasets from optical satellite observations as it is less affected by cloud cover, which enables a consistent long-term analysis of changes in global GPP. In our analysis, we compare the VODCA2GPP dataset mainly with other data-driven products (FLUXNET, MODIS, and FLUXCOM). However, FLUXCOM does not account for CO_2 fertilization effects (Walker et al., 2020), which is why trends derived from FLUXCOM are not realistic (Jung et al., 2020). Therefore, we also assess monthly anomalies and long-term trends in

VODCA2GPP against TRENDY models, which consider CO_2 fertilization.

2 Data

2.1 Input to the VODCA2GPP model

2.1.1 VODCA

The Vegetation Optical Depth Climate Archive (VODCA v1; Moesinger et al., 2020) consists of three single-frequency VOD products (Ku-, X-, and C-band), covering the period from 1987–2017 (Ku-band), 1997–2019 (X-band), and 2002–2019 (C-band). For VODCA2GPP, we used an updated VODCA version (VODCA v2 CXKu; Zotta et al., 2022) that merges all bands into a single dataset to obtain increased spatial and temporal coverage and reduce random errors compared to VODCA v1. VODCA v2 CXKu utilizes observations from the same sensors and frequencies as VODCA v1 (Table 1) to generate a single long-running, multi-frequency VOD time series. VODCA v2 CXKu is obtained by first scaling VODCA v2 observations from the C- and Ku-band to the X-band to remove systematic biases and then by computing a weighted average in order to fuse overlapping observations. The reference frequency for the scaling of the different frequencies is the X-band. VODCA v2 CXKu provides a single long-term vegetation metric covering over 30 years of observations (1988–2020) and thus exceeds the temporal length of the single-frequency multi-sensor products (VODCA v2 C, X, and Ku). VODCA v2 CXKu merges 15 passive nighttime VOD datasets retrieved from seven different sensors via the Land Parameter Retrieval Model (LPRM; Van der Schalie et al., 2017). The LPRM is based on radiative transfer theory introduced by Mo et al. (1982), uses forward modelling to simulate the top-of-atmosphere brightness temperatures under a wide range of conditions, and minimizes its difference with the actual satellite observation. Although primarily developed for soil moisture, it simultaneously solves for the VOD using an analytical solution by Meesters et al. (2005), utilizing the ratio between H- and V-polarized observations (Van der Schalie et al., 2017). The LPRM assumes that the soil and vegetation temperatures are equal, which may not be the case during the day due to uneven heating from solar radiation. VODCA v2 therefore uses only nighttime observations, which are assumed to be in thermal equilibrium (Owe et al., 2008). Scaling of the single-sensor VOD observations is achieved by means of cumulative distribution function (CDF) matching (Moesinger et al., 2020).

The preprocessing of LPRM level-2 VOD data used in VODCA v2 follows the steps described in detail in Moesinger et al. (2020). These include projecting the data onto a $0.25° \times 0.25°$ grid, using nearest-neighbour resampling, and selecting the closest nighttime value in a window of ± 12 h for every 00:00 UTC (Zotta et al., 2022). Data are masked for radio-frequency interference (De Nijs et al., 2015), negative VOD retrievals, and temperatures. Differently from Moesinger et al. (2020), masking for low land surface temperature (LST < 0 °C), when the dielectric properties of water change drastically, is not based on Ka-band retrievals because these have high uncertainties over frozen land (Holmes et al., 2009). Instead, VODCA v2 uses the ERA5-Land (Muñoz-Sabater et al., 2021) soil temperature level-1 (stl1) data. To ensure that all observations taken under frozen conditions are masked, all observations with an associated surface soil temperature (stl1) below 3 °C are masked (Zotta et al., 2022).

2.1.2 ERA5-Land – 2 m air temperature

The 2 m air temperature (T2m) from the ERA5-Land dataset was used to represent the temperature dependence of autotrophic respiration. T2m is a commonly used parameter for describing the relationship between autotrophic respiration and temperature (Teubner et al., 2021; Drake et al., 2016; Ryan et al., 1997). ERA5-Land is a reanalysis dataset of meteorological variables which is provided by the European Centre for Medium-Range Weather Forecasts (ECMWF) (Muñoz-Sabater et al., 2021). ERA5-Land is produced at a spatial resolution of 9 km ($\sim 0.08°$) and is available hourly.

2.1.3 FLUXNET2015 in situ GPP

In situ GPP data from Tier 1 v1 FLUXNET2015 (Pastorello et al., 2020) were used to train and evaluate the VODCA2GPP product. FLUXNET GPP estimates are available for nighttime and daytime flux partitioning, which were averaged as suggested by Pastorello et al. (2020). FLUXNET data are available daily from 1991 until 2014 with a mean observation time span of 7.27 ± 4.89 years for the stations used, indicating significant variability in station data availability. An overview of the FLUXNET2015 stations used can be found in Table B1.

2.2 Reference datasets

2.2.1 MODIS GPP

GPP estimates derived from MODIS satellite data are based on Monteith's (1972) light-use efficiency concept which relates the amount of absorbed solar radiation to vegetation productivity. The MODIS algorithm uses fAPAR as a proxy for the absorbed solar energy. For this study the MOD17A2H v006 GPP product was used (Running et al., 2015; Zhao et al., 2005). It is available at an 8 d temporal resolution and 500 m sampling and was resampled to 0.25° to match the resolution of VODCA2GPP.

2.2.2 FLUXCOM GPP

FLUXCOM GPP (Tramontana et al., 2016; Jung et al., 2020) is produced by upscaling GPP estimates from in situ

Table 1. Input data for the merged-band VODCA v2 with the main sensor specifications: time periods used, local ascending equatorial crossing times (AECTs), and frequencies used. Table information is taken from Moesinger et al. (2020) and adapted for VODCA v2 CXKu.

Sensor	Time period used	AECT	C-band [GHz]	X-band [GHz]	Ku-band [GHz]	Reference
AMSR-E	Jun 2002–Oct 2011	13:30	6.93	10.65	18.70	Van der Schalie et al. (2017)
AMSR2	Jul 2012–Dec 2020 Jul 2012–Aug 2017 (Ku-band)	13:30	6.93, 7.30	10.65	18.70	Van der Schalie et al. (2017)
SSM/I F08	Jul 1987–Dec 1991	18:15			19.35	Owe et al. (2008)
SSM/I F11	Dec 1991–May 1995	17:00–18:15			19.35	Owe et al. (2008)
SSM/I F13	May 1995–Apr 2009	17:45–18:40			19.35	Owe et al. (2008)
TMI	Dec 1997–Apr 2015	Asynchronous		10.65	19.35	Owe et al. (2008), Van der Schalie et al. (2017)
WindSat	Feb 2003–Jul 2012	18:00	6.80	10.70	18.70	Owe et al. (2008), Van der Schalie et al. (2017)

eddy covariances using machine learning techniques. Two FLUXCOM GPP setups exist: FLUXCOM RS uses high-resolution land surface properties from MODIS observations as machine learning model input, while FLUXCOM RS + METEO uses the mean seasonal cycle of land surface variables derived from MODIS observations and additionally incorporates meteorological data (Jung et al., 2020). For validating VODCA2GPP, FLUXCOM RS was used because it includes temporal properties of land surface variables at a finer spatial and temporal resolution than FLUXCOM RS + METEO. FLUXCOM RS GPP has 10 km sampling and is available every 8 d in accordance with the MODIS input data. The data were aggregated to 0.25° to match the VODCA2GPP resolution.

2.2.3 TRENDY-v7 GPP

In addition to remote-sensing-based datasets, GPP estimates from the reanalysis-driven TRENDY-v7 ensemble of 16 dynamic global vegetation models (DGVMs) were used as an independent reference dataset (Le Quéré et al., 2018; Sitch et al., 2015). TRENDY-v7 simulations consider forcing effects of climate, land use, and changes in atmospheric CO_2 concentration on GPP over the period 1950–2017. The TRENDY-v7 ensemble consists of the following DGVMs: CABLE-POP, CLASS-CTEM, CLM5.0, DLEM, ISAM, JSBACH, JULES, LPJ, LPJ-GUESS, LPX, OCN, ORCHIDEE, ORCHIDEE-CNP, SDGVM, SURFEX, and VISIT. DGVMs output monthly GPP, which was provided on a common $1° \times 1°$ grid. For the comparison with VODCA2GPP, all TRENDY-v7 models were regridded to 0.25° using nearest-neighbour resampling and merged into an unweighted ensemble mean GPP time series.

3 Methods

3.1 VOD2GPP model

VODCA2GPP is based on the VOD-driven GPP estimation approach (the VOD2GPP model) introduced by Teubner et al. (2019, 2021). The VOD2GPP model describes the theoretical relationship between GPP and VOD. The biogeochemical basis of this model is the relationship between GPP and ecosystem net uptake of carbon (NPP) and autotrophic respiration (R_a) (Bonan, 2008):

$$\mathrm{GPP} = R_a + \mathrm{NPP}, \quad (1)$$

where R_a can be again split into two terms: maintenance respiration and growth respiration (Bonan, 2008). The VOD2GPP model makes use of several VOD variables to represent the sum of NPP and R_a: the original VOD time series (VOD), which relates to maintenance respiration; temporal changes in VOD (Δ(VOD)), which relate to both growth respiration and NPP; and the temporal median of VOD (mdn(VOD)) derived from the complete time series, which serves as a proxy for vegetation density. Specifically, mdn(VOD) is incorporated to subtract larger structural vegetation components which makes the resulting model more closely related to biomass changes of smaller structural vegetation components such as leaves. It was shown that this increases model performance (Teubner et al., 2019). NPP is mostly represented by Δ(VOD), while R_a is represented by the original VOD signal and Δ(VOD). Thus, the VOD-based-only VOD2GPP model can be formulated as follows (Teubner et al., 2019):

$$\mathrm{GPP(VOD)} = s(\mathrm{VOD}) + s(\Delta(\mathrm{VOD})) + s(\mathrm{mdn(VOD)}), \quad (2)$$

where $s()$ denotes the mapping function that maps the input variables to GPP. Δ(VOD) is derived for each pixel (x_i) by

computing the difference between two consecutive VOD observations of the smoothed and 8 d aggregated VOD signal (Teubner et al., 2019):

$$\Delta(\mathrm{VOD}) = \mathrm{VOD}_{x_i,t_j} - \mathrm{VOD}_{x_i,t_{j-1}} .$$

The smoothing was performed in order to increase the robustness of the derivation and implemented using a Savitzky–Golay filter with a window size of 11 data points as suggested by Teubner et al. (2021).

Equation (2) represents a simplified model formulation connecting VOD to GPP but does not explicitly take into account the strong temperature dependence of autotrophic respiration (Wythers et al., 2013; Atkin et al., 2005; Tjoelker et al., 2001), which is mainly attributed to its maintenance part (Bonan, 2008; Ryan et al., 1997). Therefore, an improved formulation of the model was developed by considering the temperature dependence of maintenance respiration through a term representing the interaction between temperature (T2m) and VOD (Teubner et al., 2021):

$$\begin{aligned}\mathrm{GPP}(\mathrm{VOD},\mathrm{T2m}) = {} & te(\mathrm{VOD},\mathrm{T2m}) + s(\Delta(\mathrm{VOD})) \\ & + s(\mathrm{mdnVOD}). \end{aligned} \quad (3)$$

The mapping and interaction functions were implemented using generalized additive models (GAMs). The usage of short time intervals (on the order of several days) for the computation of Δ(VOD) is crucial since it reduces the influence of larger vegetation components (e.g. stems) and makes the model more sensitive to changes in leaf biomass.

3.2 Generalized additive models

Generalized additive models (GAMs; Hastie and Tibshirani, 1990) are semi-parametric generalizations of linear models and combine properties of generalized linear models (GLMs) and additive models (Guisan et al., 2002). Link functions $f()$ are trained and summed up for each predictor in order to relate the expected value of a response variable $E(Y)$ to the explanatory variables x_i (Hastie and Tibshirani, 1990). The model can be written as

$$E(Y) = \beta + \sum_{i=1}^{n} s_i(x_i), \quad (4)$$

where β denotes a constant offset and n corresponds to the number of input predictor variables x_i. The link functions $s_i()$ are implemented as smooth spline functions and allow the representation of non-monotonic and non-linear relationships, which give them a high degree of flexibility (Hastie and Tibshirani, 1990). Hence, the relationship between target and predictor variables does not require explicit a priori knowledge but can be estimated from the data themselves, which makes GAMs appropriate for the VOD2GPP model for which the exact relationship between VOD, air temperature, and GPP is difficult to determine (Teubner et al., 2019).

3.3 Preprocessing

The model input data (response variable, FLUXNET GPP; predictor variables, VODCA v2 CXKu, ERA5-Land T2m) were resampled from a daily to 8 d resolution using the 8 d means over the respective time period in order to reduce noise and computation times. This also means that the final VODCA2GPP represents the mean of daily GPP for an 8 d period with an estimate every 8 d. Since VODCA v2 CXKu already incorporates extensive quality flagging (e.g. for temperature), no additional data processing was necessary.

3.4 Model training and output

For each valid FLUXNET2015 in situ observation, the corresponding overlapping pixel values of VOD, Δ(VOD), mdn(VOD), and T2m were used to set up the GAM. Data from days with at least one invalid or missing observation were not considered for model training. While cross-validation was performed to evaluate the model (Sect. 3.5), all data were used for training of the final VODCA2GPP model. The GAM-based implementation of the VOD2GPP model is consistent with Teubner et al. (2021) and utilizes algorithms from the pyGAM Python package (Servén and Brummitt, 2018).

The trained VODCA2GPP model was applied to each pixel where all input variables (VOD, Δ(VOD), mdn(VOD), and T2m) were available. The result of this upscaling process is VODCA2GPP, which covers the period between January 1988 and July 2020. It has a spatial resolution of 0.25°, and its temporal resolution is 8 d. In rare cases ($\sim$ 2.5 % of all data points) the machine learning model produced slightly negative results for GPP due to the extrapolation capacities of the trained GAM. As negative GPP is not possible, such estimates were set to zero.

3.5 Site-level evaluation and uncertainty assessment

The robustness of the model was evaluated based on a site-based cross-validation analysis during which the influence of the selection of available in situ stations on the GPP model was investigated. For the cross-validation 10 VODCA2GPP models were trained. Each of the 10 models was trained with 90 % of the available FLUXNET stations, while the remaining 10 % of the stations were retained for validation (Teubner et al., 2019). Every station was excluded exactly once, which is why this approach is classified as pseudo-random. Model performance was assessed at all sites that were omitted in the respective model run by computing root mean square errors (RMSEs), bias, and Pearson's r for different timescales (8 d, monthly, and yearly). In addition, the uncertainty in the VODCA2GPP model was then expressed through the minimum–maximum range as well as the standard deviation of the resulting 10 mean annual accumulated GPP estimates for each pixel. The standard deviation is also incorporated as an uncertainty map in the available dataset (layer name

"Uncertainties") to support users with an indicator for known uncertainties in VODCA2GPP.

3.6 Product evaluation and assessment

Mean annual, monthly, and 8 d GPP from VODCA2GPP, MODIS GPP, and FLUXCOM GPP was evaluated against GPP from FLUXNET. The error metrics used were RMSE, bias, and Pearson's r. Global spatial GPP patterns were compared against products by computing the mean annual GPP per pixel and the differences in mean annual GPP per pixel over the common observation period. Temporal agreements were tested by means of a Pearson correlation analysis for 8 d GPP. A correlation analysis of GPP anomalies was conducted for monthly GPP and also includes TRENDY-v7 GPP, which only provided monthly GPP data. Anomalies were derived by subtracting the long-term mean of the overlapping observation periods from monthly GPP estimates for each product.

Additionally, a trend analysis was conducted for all available GPP products in order to compare long-term changes in GPP. Trends in yearly median GPP were quantified using the Theil–Sen estimator (Theil, 1950; Sen, 1968), which calculates the slopes for each line between two points. The median of all computed slopes is then used for line fitting, making it insensitive to outliers and more robust than simple linear regression (Wilcox, 2010). Slopes were considered significant when the signs of the lower and upper 90 % confidence intervals were equal. For the trend analysis, yearly median GPP was used.

4 Results

4.1 Spatiotemporal patterns in global GPP

The average annual GPP of VODCA2GPP exhibits spatial patterns similar to the remote-sensing-based MODIS and FLUXCOM products (Fig. 1). The agreement in annual GPP is high in northern latitudes (e.g. Europe, Russia, Canada), while there are relatively large differences in the Southern Hemisphere, especially in tropical and sub-tropical regions (Fig. 1d). The largest positive differences are found in the sub-tropics. Very arid regions (e.g. Australian deserts, Kalahari Desert) have low mean yearly productivity in all three datasets (Fig. 1a) but tend to be higher in VODCA2GPP compared to MODIS and FLUXCOM (Fig. 1b and c). The mean global total GPP as derived from VODCA2GPP amounts to $200 \pm 2.2\,\mathrm{Pg\,C\,yr^{-1}}$. Comparison of the latitudinal distribution of FLUXNET stations shows that the closest agreement in yearly GPP is generally found in regions with a high density of FLUXNET in situ stations, while the largest discrepancies are found in regions with few or no FLUXNET stations.

Similarly, uncertainties tend to be smaller in latitudes with a high density of FLUXNET stations (Fig. 1d). The lowest spread in the 10 models (i.e. the lowest uncertainty) is found north of 20° N where the majority of FLUXNET GPP stations are also located. The Southern Hemisphere, where only a few in situ stations are located, generally exhibits a larger spread (higher uncertainty), indicating a considerable sensitivity of the model to the choice of stations. This emphasizes the need for a well-distributed network of in situ flux towers across all biomes. The uncertainty map (Fig. 2b) shows that arid regions (e.g. Sahara, Australian deserts, Arabian Peninsula) as well as various mountainous regions (e.g. Carpathians, Alps, Rocky Mountains, Andes) have the highest model uncertainties. Moderate to high model uncertainties are also exhibited for the tropics. Furthermore, significant uncertainties in VODCA2GPP are found in parts of eastern and western Siberia's boreal forests as well as in parts of southern China.

VODCA2GPP shows good temporal agreement with MODIS and FLUXCOM for most regions outside the tropics (Fig. 3). Pearson's r is the highest in regions with distinct interannual variability such as sub-arctic, temperate, and semi-arid regions and the lowest for dense tropical forests where even negative correlations occur. The median Pearson's r values between VODCA2GPP and the reference datasets MODIS and FLUXCOM are 0.77 and 0.75, respectively.

4.2 Site-level evaluation

VODCA2GPP's tendency towards a positive bias with respect to MODIS and FLUXCOM products is not mirrored in the comparison against FLUXNET GPP (Figs. 4 and A1). The bias with respect to FLUXNET site data is substantially smaller for VODCA2GPP than for MODIS and FLUXCOM. The RMSE and Pearson's r values of VODCA2GPP are slightly higher and lower, respectively, than for MODIS and FLUXCOM and are of the same magnitude for 8 d values and mean annual GPP. All three datasets underestimate productivity at high GPP values. A land-cover-based analysis (Fig. A3) shows that discrepancies in annual VODCA2GPP mostly occur in (semi-)arid environments (e.g. savannas, open shrublands, grasslands). VODCA2GPP performs best in temperate environments (e.g. wetlands, evergreen broadleaf forest, croplands). Wetlands and evergreen broadleaf forests exhibit the best performance for all products, while all three datasets underperform in open shrublands and deciduous broadleaf forest.

The site-based spatial cross-validation also exhibits only a small (negative) bias of VODCA2GPP (Fig. 5) for monthly and 8 d GPP values, while the bias for annual variations is positive and slightly higher. A high median Pearson's r for 8 d and monthly values indicates good model performance for seasonal variations. It is to be noted that there are only eight significant Pearson's r values for yearly sampling, which decreases the expressiveness of this value. This is explicable with the short observation period of most FLUXNET sites which might not exhibit interannual vari-

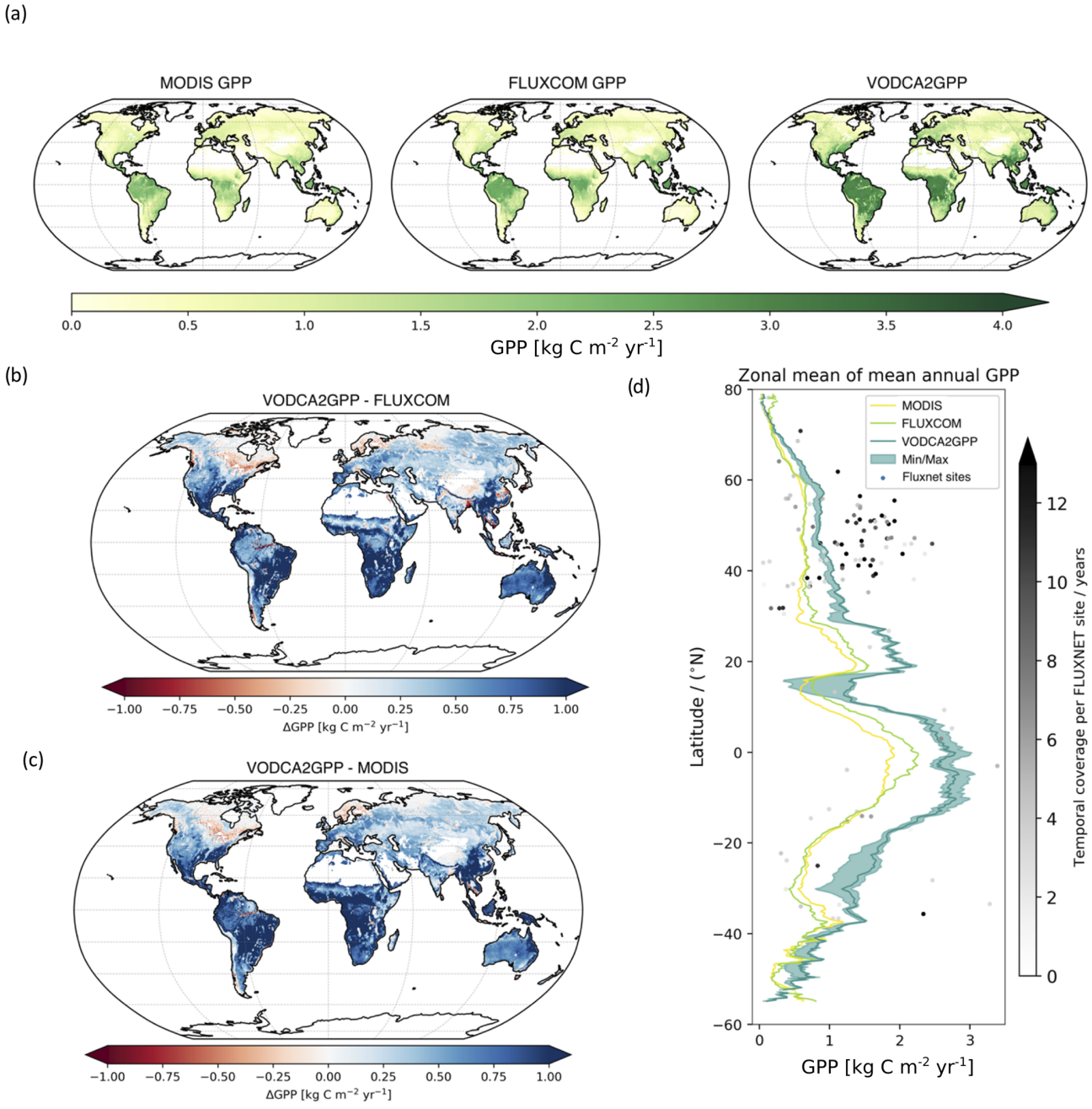

Figure 1. **(a)** Mean yearly aggregated GPP for the common observation period of the three products VODCA2GPP, MODIS, and FLUXCOM (2002–2016); **(b, c)** difference in mean annual GPP between VODCA2GPP and FLUXCOM and MODIS, respectively; **(d)** latitude plot of zonal means of mean annual GPP. The means were computed based on 8 d, 0.25° sampling. The Min/Max area denotes the minimum–maximum latitudinal mean for the 10 model runs that were obtained with the site-based cross-validation. The dots represent the latitudinal location of the FLUXNET sites and their corresponding mean annual GPP. The brightness of the dots indicates the data availability for the respective FLUXNET station. Only pixels and observation dates that are available in all three datasets were used for these plots.

ability. The RMSE decreases with increasing observation length scales.

4.3 Anomaly patterns in space and time

In terms of anomalies from the long-term climatology, VODCA2GPP shows good correlation with MODIS and TRENDY-v7 and weaker correlation with FLUXCOM (Table 2, Fig. 6). TRENDY-v7 correlates similarly well with

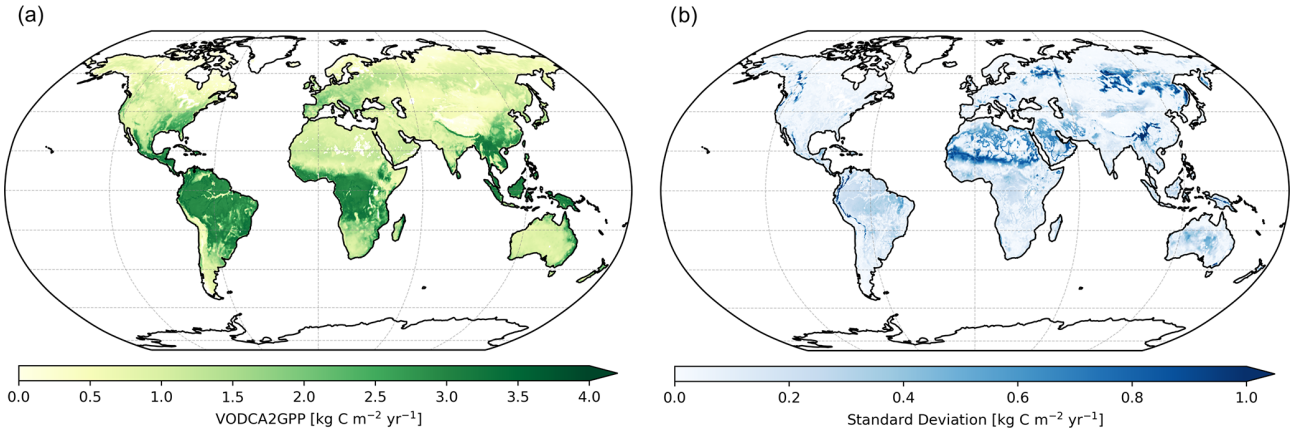

Figure 2. **(a)** Mean annual GPP as derived from VODCA2GPP for the period 1988–2019. **(b)** Standard deviation of mean annual GPP (1988–2019) as obtained by the uncertainty analysis based on site-level cross-validation.

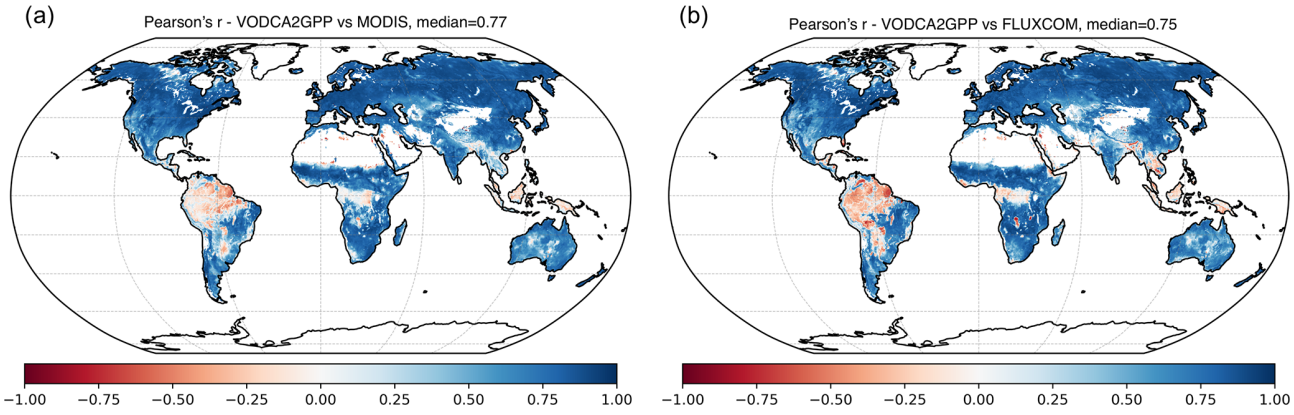

Figure 3. Pearson's r between VODCA2GPP and MODIS GPP **(a)** and VODCA2GPP and FLUXCOM GPP **(b)**. The correlations are based on the common observation period between 2002 and 2016 with a 0.25° spatial and 8 d temporal resolution.

VODCA2GPP, and MODIS and shows worse correspondence with FLUXCOM. The highest correlation is found between the two products based on optical remote sensing: MODIS and FLUXCOM.

The temporal evolution and spatial distribution of the anomalies exhibit similar patterns (Fig. A4). Several extreme events are captured in VODCA2GPP and in at least one of the other GPP datasets. An example of such GPP extremes is the strong positive anomalies between 2010 and 2011 at around 25° S which were mainly caused by record-breaking rainfalls in Australia (Wardle et al., 2013). These positive anomalies are clearly visible in all examined GPP products apart from FLUXCOM (Fig. A4). Other GPP extremes that are noticeable in all products apart from FLUXCOM are the extremely low GPP in 2002, 2003, and early 2005 around 20° S (Fig. A4). Both anomalies can be explained by extreme drought events that occurred in these years (Bureau of Meteorology, 2002, 2003, 2005; Horridge et al., 2005), which are associated with El Niño events (Taschetto and England, 2009). Also, the distinct drop in GPP in 2015 and 2016 in similar latitudes is likely linked to El Niño-related drought events (Malhi et al., 2018; Zhai et al., 2016). Generally, extreme events in VODCA2GPP are more pronounced than in the other datasets.

4.4 Global GPP trends

Trends in global annual median GPP for the overlapping period between 2003 and 2015 are similar for VODCA2GPP, TRENDY-v7, and MODIS, and all show significant positive trends (Table 3 and Fig. 7). FLUXCOM does not exhibit a significant trend. The spatial distribution of GPP trends for the period 2003–2015 (Fig. 8) exhibits many similarities between all analysed products. Large patterns of strong positive trends are, for example, found in eastern parts of Siberia and China as well as in India and North America. Patterns of negative trends are found north of the Caspian Sea in all datasets. The remote-sensing-based products exhibit distinct patterns of declining GPP in central Siberia and significantly increasing GPP in western Russia. Generally, the trends of

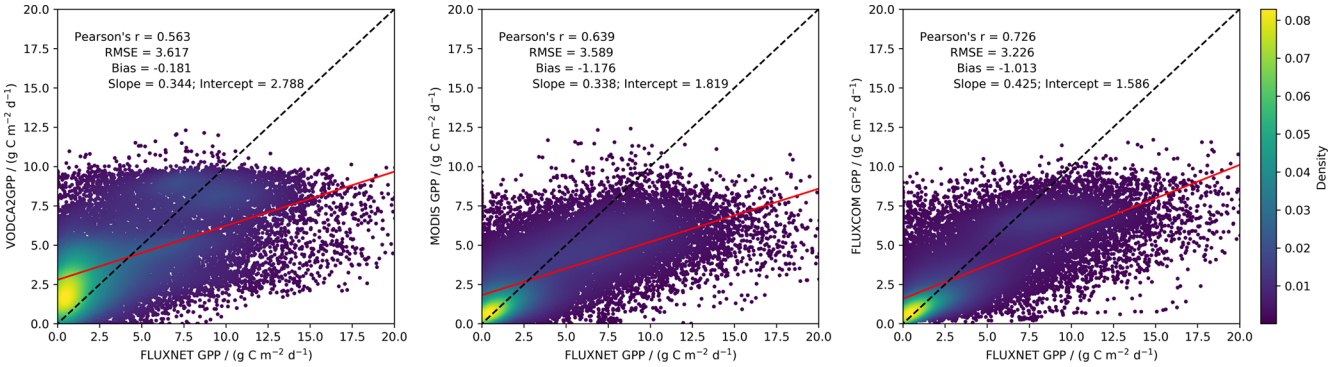

Figure 4. GPP from FLUXNET plotted against GPP from VODCA2GPP, MODIS, and FLUXCOM for the period 2002–2016 with 8 d sampling.

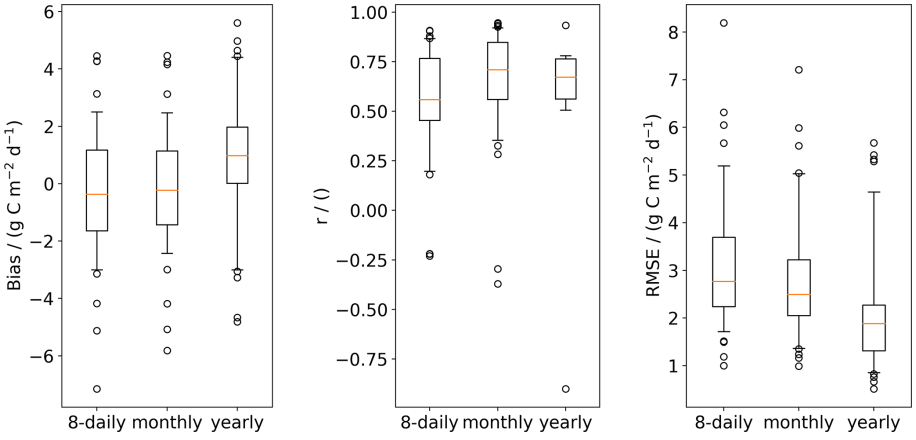

Figure 5. Site-based cross-validation for 8 d, monthly, and yearly sampling of GPP from VODCA2GPP and FLUXNET. RMSE, bias, and Pearson's r were computed at each of the 10 % of FLUXNET sites that were omitted during the respective training run. Non-significant Pearson correlations (p value < 0.1) were ignored. The boxplots for Pearson's r are based on the 71 (8 d), 66 (monthly), and 8 (yearly sampling) significant values for Pearson's r values. The whiskers of the boxplots extend to the 5th and 95th percentiles.

VODCA2GPP match better with MODIS and TRENDY-v7 than with FLUXCOM. While there are many similar patterns in the Northern Hemisphere, trends in the Southern Hemisphere do not match well or are even contradictory. Especially in the tropics, hardly any similarities are apparent. Note that the analysed time period is short and may be impacted by individual extreme events.

For the full time period (1988–2019), VODCA2GPP increases slightly on a global scale (Table 3), but this cannot be classified as significant due to contradictory upper and lower confidence intervals. The same is true for the slightly shorter period between 1988 and 2016 during which TRENDY-v7 detects a small significant positive trend on a global scale. The spatial distribution of long-term (1988–2019; Fig. 9) trends in VODCA2GPP is similar to that of the shorter period (2003–2015), but in general, long-term VODCA2GPP trends are less pronounced. The comparison of the fully overlapping period between VODCA2GPP and TRENDY-v7 (1988–2016; Fig. A5) shows that TRENDY-v7 exhibits weak but consistent positive trends for practically all biomes, while VODCA2GPP trends are spatially differing and for some regions even opposite in sign to the trends in TRENDY-v7.

A comprehensive comparison with in situ GPP trends is not possible because most FLUXNET time series are too short to derive reliable trends. However, trends that could be derived for a few stations with a long time series (Fig. A6) also suggest increasing GPP. The in situ analysis indicates that there is a comparatively good correspondence between VODCA2GPP and FLUXNET GPP trends. Together with the strong similarities between VODCA2GPP and MODIS and TRENDY GPP, this suggests that VODCA2GPP can provide a valuable contribution to the analysis of global GPP trends.

Table 2. Pearson's r correlation matrix for mean global monthly GPP anomalies between 2002 and 2016.

	VODCA2GPP	MODIS GPP	FLUXCOM GPP	TRENDY-v7 GPP
VODCA2GPP	1.00			
MODIS GPP	0.53	1.00		
FLUXCOM GPP	0.29	0.69	1.00	
TRENDY-v7 GPP	0.61	0.60	0.26	1.00

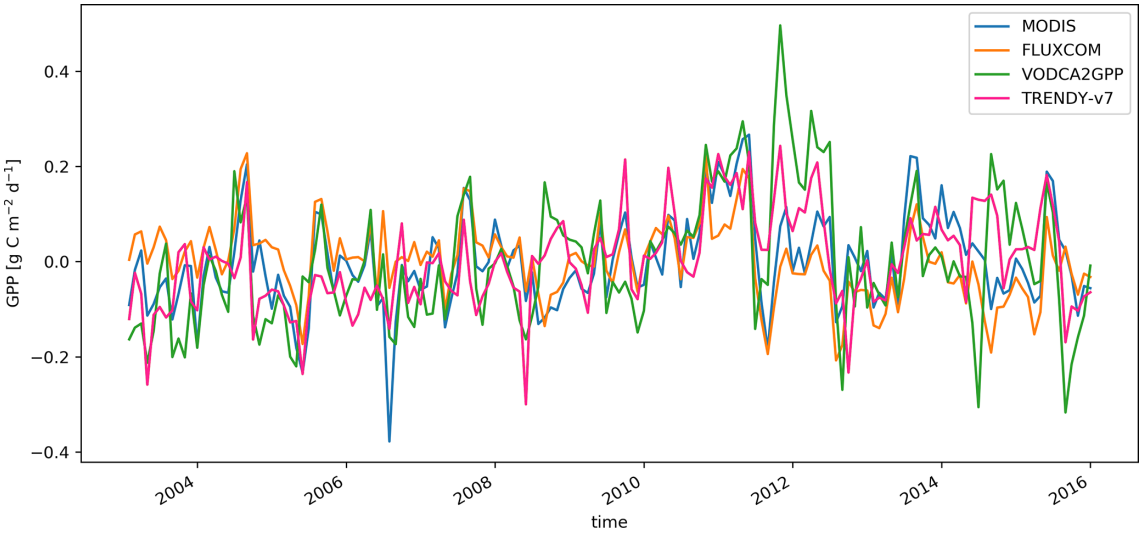

Figure 6. Time series of mean global monthly GPP anomalies.

5 Discussion

5.1 Uncertainties in the VODCA2GPP model

The results from the uncertainty analysis and the comparison with in situ GPP show that VODCA2GPP estimates can be viewed as reliable across most biomes. However, significant uncertainties were exhibited in some areas with extreme climatic or topographic conditions (e.g. deserts and mountain ranges). Also, parts of eastern and western Siberia and parts of southern China show a relatively large spread in predictions. The observed uncertainty patterns in Siberia might be associated with topography, land cover, generally lower data availability (due to frozen masking in VODCA), and a lack of FLUXNET stations. Complex topography is presumably also the main driver for uncertainties in southern China. The uncertainty analysis suggests that VODCA2GPP estimates tend to be too high in these regions and thus should be interpreted with caution. Furthermore, moderate uncertainties were also found for the tropics, which is likely due to the extremely low in situ data availability and higher absolute GPP than in mid-latitudes.

The comparison with in situ GPP shows clear differences in performance of the VODCA2GPP model across different biomes. High performance is achieved in densely vegetated biomes, while performance decreases in arid and less vegetated regions. A reason for the weaker performance in areas with less water availability might be adapted water regulation strategies of plants. Plants in drought-prone regions often reduce transpiration by limiting stomatal conductance to maintain a constant water potential even in times of extreme water scarcity (Sade et al., 2012). Since VOD is largely driven by the vegetation's water content, this isohydric behaviour of vegetation could at least partly explain relatively high VOD and consequently also overestimated GPP in those regions (Teubner et al., 2021).

Also, the observation bias which is introduced by unevenly distributed FLUXNET sites decreases the model's robustness. GPP is measured in situ only at a few locations, and these stations are mostly located in temperate regions (e.g. Europe and North America) while semi-arid and tropical forest regions are underrepresented in the training data.

A comparison of uncertainties between VODCA2GPP and GPP based on optical remote sensing (Xie et al., 2021) shows that in both cases topographic complexity decreases the reliability. Furthermore, the reliability of GPP estimates based on optical remote sensing is highly dependent on weather and illumination conditions. Clouds often contaminate or prevent the observations, which is presumably the main reason why the largest uncertainties for FLUXCOM and MODIS are found in the wet tropics where GPP is known to be underestimated (de Almeida et al., 2018; Jung et al., 2020). In

Table 3. Theil–Sen trends in global yearly median GPP. Same signs of the upper and lower 90 % confidence interval indicate significant trends. The analysed periods are 2003–2015, which corresponds to the fully overlapping periods for all datasets (for the period 2002–2016 there were some data gaps in the MODIS and FLUXCOM data used at the very beginning/very end; since these data gaps could potentially impact the slope estimation, the slightly shorter period 2003–2015 was used); 1988–2016, which corresponds to the fully overlapping period of VODCA2GPP and TRENDY-v7; and 1988–2019, which corresponds to all available complete years of VODCA2GPP data.

	2003–2015		1988–2016		1988–2019	
	Theil–Sen slope [$g C m^{-2} yr^{-1}$]	Lower/upper confidence interval	Theil–Sen slope [$g C m^{-2} yr^{-1}$]	Lower/upper confidence interval	Theil–Sen slope [$g C m^{-2} yr^{-1}$]	Lower/upper confidence interval
VODCA2GPP	0.013	+0.008/+0.025	0.002	−0.001/+0.006	0.002	−0.001/+0.005
TRENDY-v7 GPP	0.017	+0.006/+0.026	0.004	+0.000/+0.008	–	–
MODIS GPP	0.012	+0.002/+0.020	–	–	–	–
FLUXCOM GPP	−0.004	−0.009/+0.001	–	–	–	–

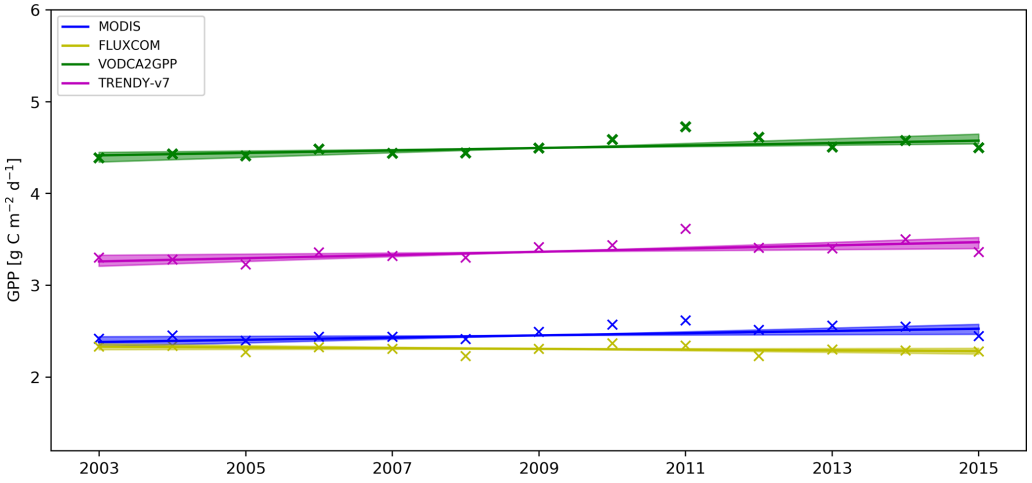

Figure 7. Time series of yearly median GPP with the regression lines as obtained by the Theil–Sen estimator. Areas around the regression lines indicate the 90 % confidence intervals.

contrast, VODCA2GPP shows good skill for densely vegetated areas, including broadleaf evergreen forests. On the other hand, the relatively high uncertainties in VODCA2GPP in water-limited regions have not been reported for FLUXCOM or MODIS GPP, indicating that these are VOD-specific and presumably caused by the above-mentioned isohydric behaviour of plants in arid regions.

5.2 Limitations in VODCA and their impact on VODCA2GPP

Certain limitations in the VODCA v1 product exist, as outlined in Moesinger et al. (2020), which are partly also evident in VODCA v2 (Zotta et al., 2022) and thus propagate to VODCA2GPP. A known issue of VODCA v2 is caused by an observation gap between October 2011 and July 2012 for AMSR-E and AMSR2 (Table 1), which prevents a direct bias removal between the sensors. However, scaling between the sensors is achieved by using TMI observations north/south of 35° N/35° S for the X- and Ku-band. Beyond these latitudes for the X- and Ku-band and globally for the C-band, AMSR-E data were matched directly to AMSR2 using the last 2 years of AMSR-E and first 2 years of AMSR2 as the reference period, under the assumption that trends between 2010–2014 are negligible (Moesinger et al., 2020). The result is that AMSR2 observations exhibit a slight positive bias in parts of North America, which is also evident in a spatial break in VODCA v1 X- and Ku-band trends (Moesinger et al., 2020). Although the impact of this procedure on VODCA2GPP trends is small and spatially limited, users are advised to keep the potential bias in mind when analysing VODCA2GPP data after 2012 for latitudes north/south of 35° N/35° S. Other limitations in VODCA concern the mixing of observations that were retrieved at different geometries (e.g. incidence angles) or observation times (Moesinger et al., 2020) and the data loss in certain regions, mostly in the Himalayas, which is caused by failure of the CDF-matching method due to insufficient input data (Moesinger et al., 2020). These issues, however, only have a small or spatially very limited influence on the final VODCA2GPP product. Furthermore, VOD retrievals exhibit a tendency towards saturation in regions with very dense vegetation, mak-

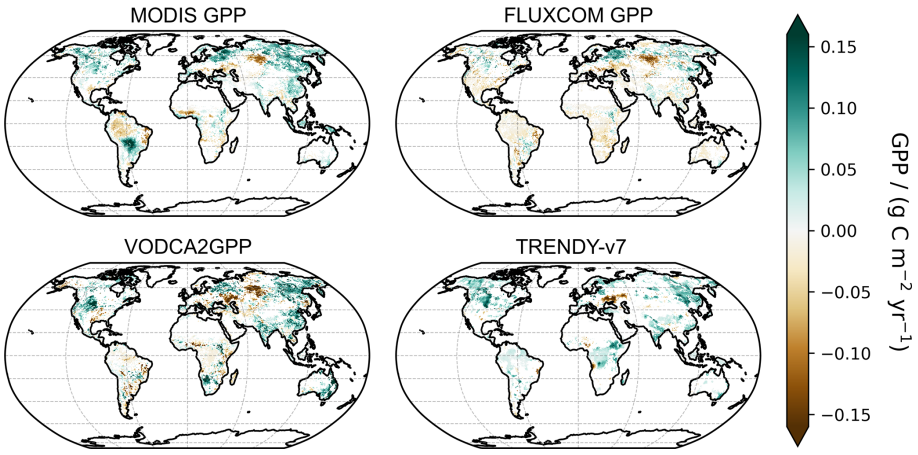

Figure 8. Global map of trends in yearly median GPP for the period 2003–2015 for all analysed datasets. White indicates non-significant trends.

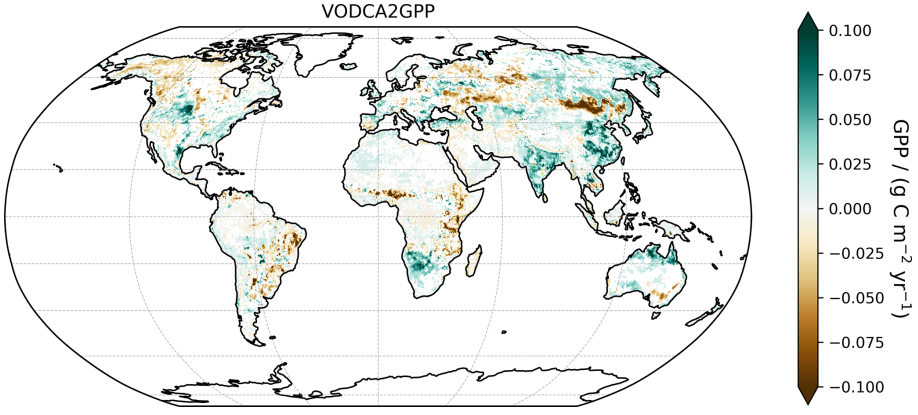

Figure 9. Global map of yearly median GPP trends for the period 1988–2019 for VODCA2GPP. White indicates non-significant trends.

ing it less likely to distinguish variability. A slight tendency towards saturation was also observed for VODCA2GPP, but the land-cover-based analysis exhibited a very high agreement between VODCA2GPP and in situ GPP, indicating high reliability of VODCA2GPP over densely vegetated regions.

Another limitation of VOD products in general, and thus also of VODCA2GPP, is the limited spatial resolution (0.25°). The lower spatial granularity achieved from passive microwave remote sensing is presumably another reason for the slightly weaker performance of VODCA2GPP in comparison with GPP derived from optical remote sensing since the VODCA grid cell might not always be well represented by the in situ measurements. Furthermore, the lower spatial resolution of VODCA2GPP is disadvantageous for the analysis of local GPP as small-scale variations in GPP might be hidden in VODCA2GPP. However, due to its long-term availability and generally high reliability, VODCA2GPP can still serve as a valuable source of data for various other applications (Sect. 5.4), especially concerning long-term climate-related studies and climate model evaluation.

5.3 Observed bias between VODCA2GPP and other remote-sensing-based GPP datasets

There is only a very small bias when comparing VODCA2GPP with eddy-covariance measurements from FLUXNET, but relatively large discrepancies in absolute GPP exist between VODCA2GPP and other remote-sensing-based products and to a lesser extent with process-based TRENDY-v7 models. In tropical regions, the positive bias between VODCA2GPP and MODIS and FLUXCOM GPP can be partly explained by a reported and observed tendency of FLUXCOM and MODIS to underestimate GPP in these regions (Turner et al., 2006; Wang et al., 2017; Figs. 1 and A3). Outside the tropics, discrepancies in absolute GPP among products might be caused by the assumed overestimation of VODCA2GPP in winter months (i.e. in times with very little or no primary productivity). This overestimation is explained by water content in vegetation that is also present in these dormant periods. The sensitivity of microwaves to this water content results in non-zero VOD and, consequently, non-zero GPP (Teubner et al., 2021). This effect is similar to the isohy-

dricity effect discussed in Sect. 5.1, which is an explanation for overestimation of VODCA2GPP in arid regions.

Another potential explanation for the positive bias of VODCA2GPP compared to MODIS and FLUXCOM is the presence of surface water and its impact on VOD retrievals. The presence of surface water is known to decrease the brightness temperature of the earth's surface and thus significantly decreases VOD retrievals (Bousquet et al., 2021). The impact of surface water contamination is evident in VODCA pixels that partly contain waterbodies (e.g. lakes, rivers). These pixels exhibit systematically lower values than neighbouring pixels without waterbodies. On the one hand, this leads to underestimation in the VODCA2GPP model in pixels containing surface water. On the other hand, it also has an effect on model training. This effect is caused by FLUXNET stations located close to waterbodies, which hardly impacts in situ GPP retrievals but does cause erroneous VOD retrievals at the 0.25° pixel scale. As a result, underestimated VOD is trained against unaffected in situ GPP, which causes a slight but systematic global overestimation. A potential solution would be the masking of water-contaminated VOD. However, due to the constraints with temperature in the interaction term (Eq. 3), this would strongly reduce the data available for training, which would potentially decrease the robustness of the VODCA2GPP model if the number of stations is not increased.

A general issue in the upscaling of GPP is the low availability of in situ GPP, which not only is problematic in model training but also hampers a fair evaluation and validation at the global scale. The remote-sensing-based reference products, FLUXCOM and MODIS, however, are also trained and calibrated using in situ GPP observations (Jung et al., 2020; Running et al., 1999) and can therefore not be viewed as fully independent from VODCA2GPP (Teubner et al., 2021). In contrast to observation-based GPP products, estimates from the TRENDY ensemble can be considered largely independent from VODCA2GPP.

5.4 Potential applications of VODCA2GPP

The validation results show that VODCA2GPP generally exhibits a high consistency with in situ GPP observations and global state-of-the-art GPP products, indicating that VODCA2GPP can be used complementarily to current global GPP products. For the analysis of global as well as regional GPP anomalies, VODCA2GPP can provide valuable insights that might be hidden in other observational products due to the fundamentally differing observation methods and the associated limitations related to saturation effects, cloud cover, and other atmospheric effects such as water vapour content or aerosols (Xiao et al., 2019).

Also, for the monitoring of global GPP trends, VODCA2GPP has the potential to serve as an independent and reliable source of data. The long-term trend analysis suggests that the majority of biomes have increased their primary productivity since 1988. There are several potential drivers for long-term increases in GPP, the most important ones being global warming, land-use changes, and elevated CO_2 concentration in the atmosphere (Piao et al., 2019). The observed long-term trends in GPP across the different products support the theory of elevated atmospheric CO_2 leading to an increased uptake of CO_2 (Haverd et al., 2020; Walker et al., 2020; Campbell et al., 2017; Schimel et al., 2015). The absence of trends in FLUXCOM does not contradict but rather supports this theory as FLUXCOM does not account for CO_2 fertilization effects (Jung et al., 2020). Due to the shortness of most in situ GPP time series, it is, however, difficult to draw final conclusions on the existence of, magnitude of, and reasons for long-term variations in GPP. Therefore, the global influence of atmospheric CO_2 on vegetation productivity remains uncertain, but VODCA2GPP allows us to gain new perspectives on long-term GPP trends and might help to identify and quantify driving factors for increasing long-term primary productivity.

Furthermore, VODCA2GPP can be used as a largely independent source of data for the intercomparison and validation of other existing or newly developed global GPP datasets and models. Currently, a multitude of global GPP products exists showing large inconsistencies among products (Zhang and Aizhong, 2021). Similarly to other global GPP datasets, VODCA2GPP cannot be seen as a true reference, but using it as an additional reference might help to acquire a more comprehensive picture of the performance of other datasets, especially in the context of long- and short-term variability in GPP.

6 Data availability

The VODCA2GPP data can be accessed (CC BY-NC-SA 4.0) at TU Data Repository under https://doi.org/10.48436/1k7aj-bdz35 (Wild et al., 2021).

7 Conclusions

In this dataset paper we introduced VODCA2GPP, a long-term GPP data record which uses multi-sensor, multi-frequency microwave VODCA data and temperature data from ERA5-Land for the upscaling of in situ GPP from FLUXNET2015. The comparison of VODCA2GPP with FLUXNET in situ GPP and global state-of-the-art GPP datasets showed good correspondence between the products in both the spatial and the temporal domain but with varying performance differences across biomes and analysed timescales. In tropical and arid regions, VODCA2GPP has significantly higher values than the reference datasets. Arid and mountainous areas were found to have the largest uncertainties. The analysis of monthly anomalies exhibited various extreme events in VODCA2GPP that are also found

in one or more existing products, indicating high plausibility of VODCA2GPP-derived anomalies. Furthermore, trends derived from VODCA2GPP contain several plausible patterns that match those derived from the TRENDY-v7 simulations but are not visible in both observational products and vice versa. This suggests that the novel microwave-based approach in VODCA2GPP has the potential to reveal novel findings about temporal dynamics in GPP at large scales that are not yet captured by other GPP products.

Appendix A

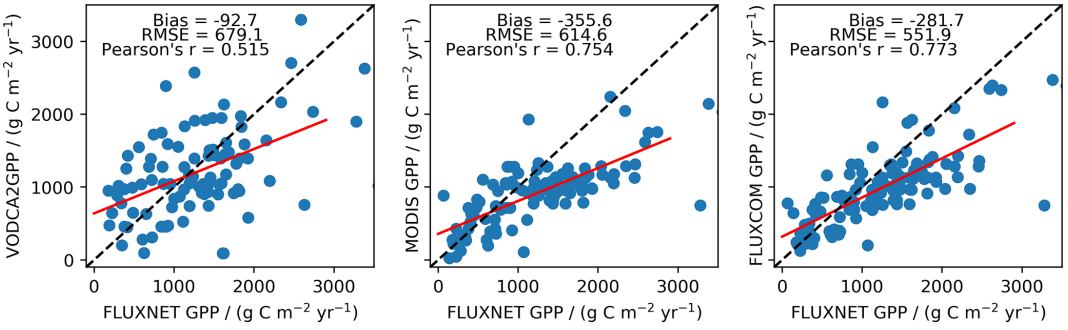

Figure A1. Mean annual in situ GPP (FLUXNET) plotted against mean annual GPP from VODCA2GPP, FLUXCOM, and MODIS for the respective grid cells. Mean annual GPP was computed from all available overlapping years, and thus each station is represented by one dot. Red lines indicate the best linear fits determined by ordinary linear regression, and the black lines represent the 1 : 1 lines.

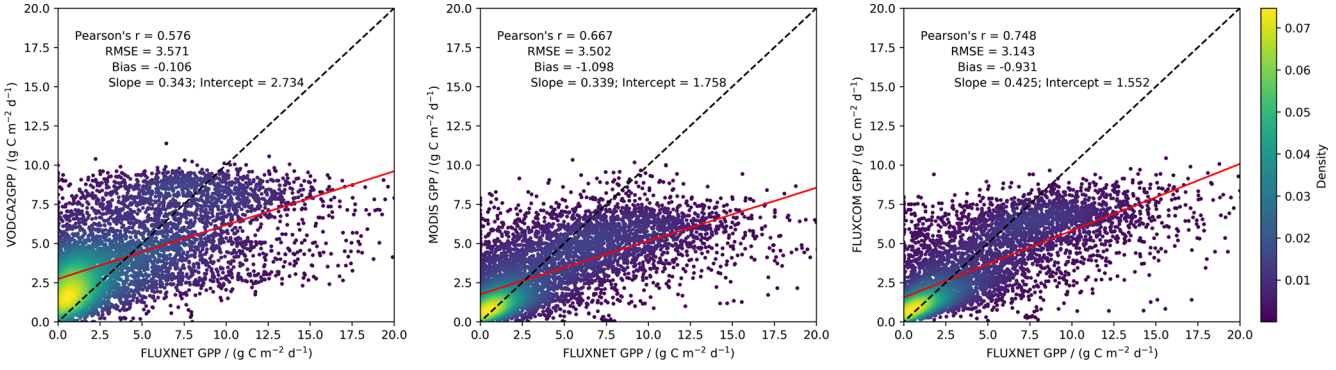

Figure A2. GPP from FLUXNET plotted against GPP from VODCA2GPP, MODIS, and FLUXCOM for the period 2002–2016 with monthly sampling.

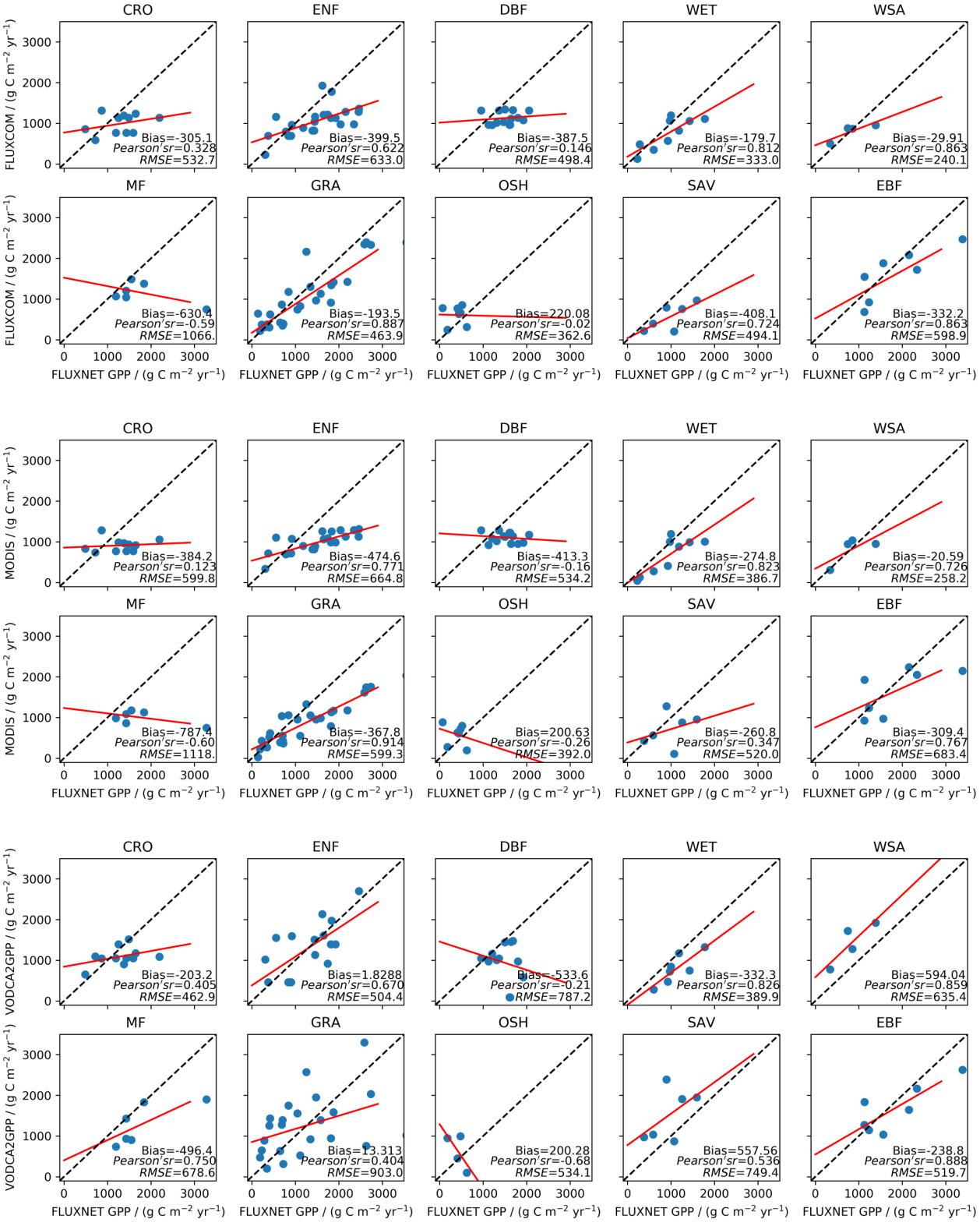

Figure A3. Scatterplots of mean annual GPP for FLUXCOM, MODIS, and VODCA2GPP for the period 2002–2016 per vegetation type. Vegetation types indicate the predominant IGBP vegetation type at the respective FLUXNET station. Abbreviations are as follows: CRO, croplands; ENF, evergreen needleleaf forests; DBF, deciduous broadleaf forests; WET, permanent wetlands; WSA, woody savannas; MF, mixed forests; GRA, grasslands; OSH, open shrublands; SAV, savannas; EBF, evergreen broadleaf forests.

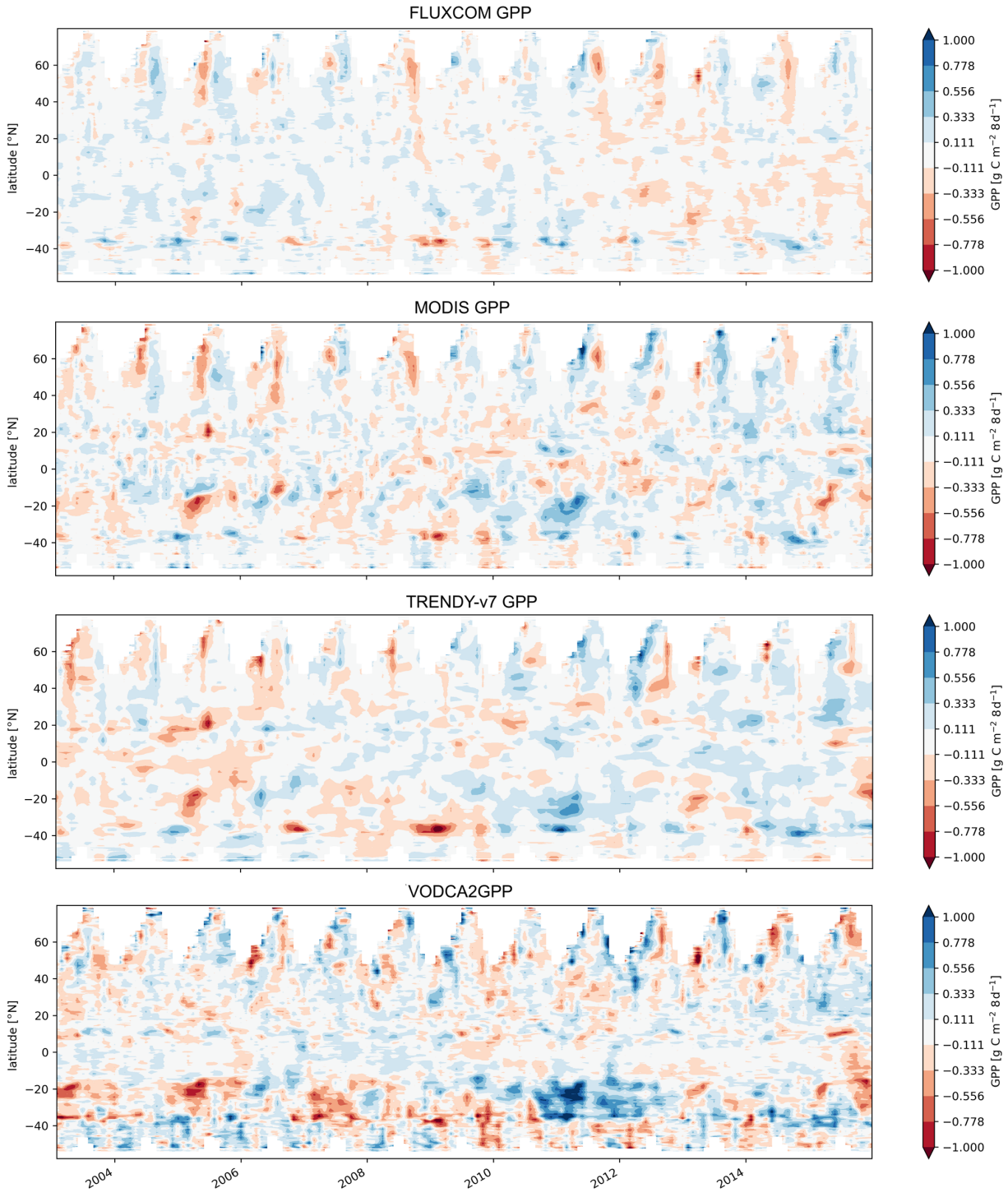

Figure A4. Hovmöller diagrams of monthly GPP anomalies for each dataset.

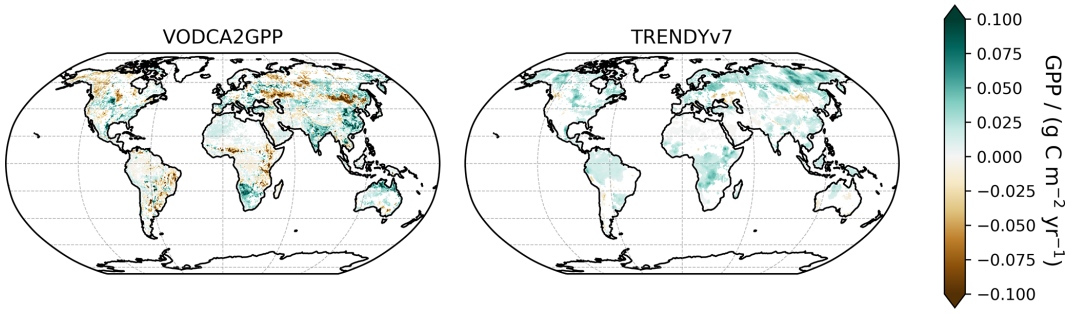

Figure A5. Global maps of yearly median GPP trends for the period 1988–2016 for VODCA2GPP and TRENDY-v7. White indicates non-significant trends.

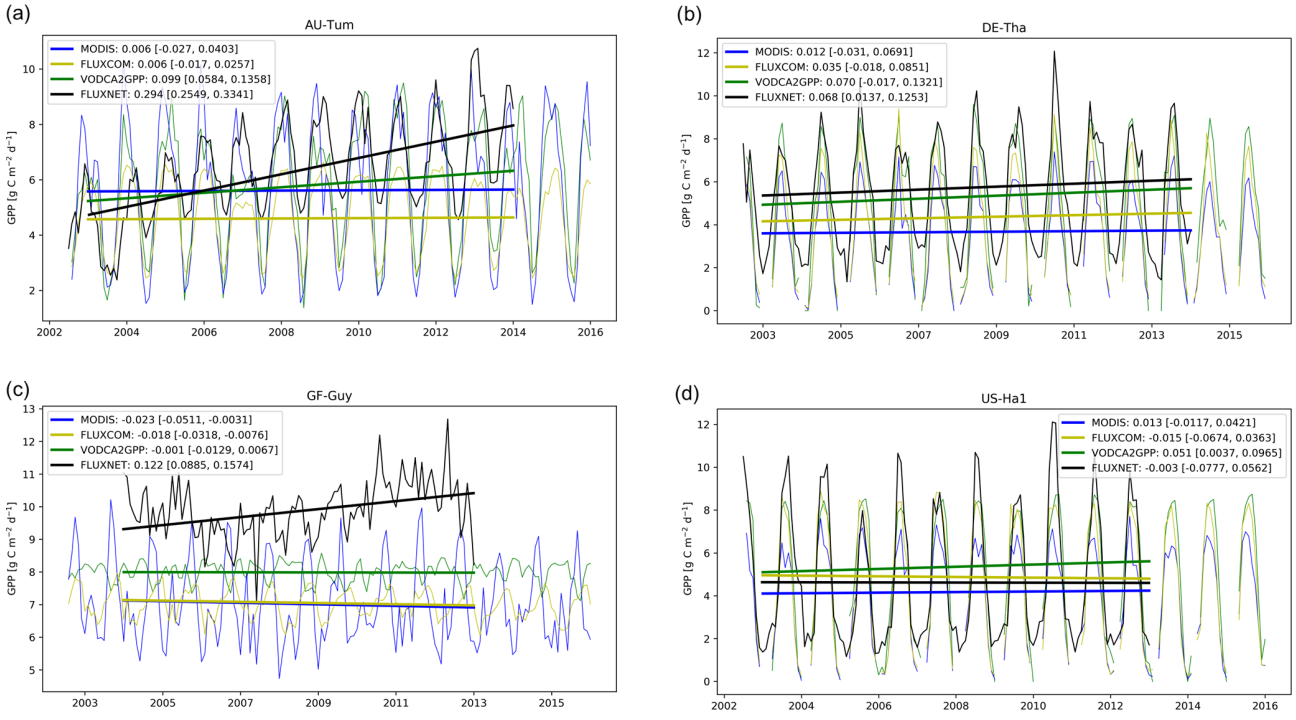

Figure A6. Exemplary collection of time series of in situ FLUXNET GPP together with extracted time series from MODIS, FLUXCOM, and VODCA2GPP. The stations were selected because of their high data availability for their respective land cover. The lines indicate the regression lines as obtained from the Theil–Sen slope estimation for yearly median GPP. The trends are computed for the common observation period with FLUXNET. The slope [g C m^{-2} yr^{-1}] is depicted in the legend together with the respective 90 % lower and upper confidence intervals. The depicted stations are as follows: **(a)** AU-Tum – Tumbarumba, Australia; −35.65° N, 148.15° E; land cover EBF; **(b)** DE-Tha – Tharandt, Germany; 50.96° N, 13.57° E; land cover ENF; **(c)** GF-Guy – Guyaflux, French Guiana; 5.28° N, −52.93° E; land cover EBF; **(d)** US-Ha1 – Harvard Forest EMS Tower, United States; 42.54° N, −72.17° E; land cover DBF.

Appendix B

Table B1. Overview of FLUXNET Tier 1 v1 stations within the period 1991–2014.

FLUXNET ID	Name	Long [° E]	Lat [° N]	Years used
AR-SLu	San Luis	−66.46	−33.46	2009–2011
AR-Vir	Virasoro	−56.19	−28.24	2010–2012
AT-Neu	Neustift	11.32	47.12	2002–2012
AU-ASM	Alice Springs	133.25	−22.28	2010–2013
AU-Ade	Adelaide River	131.12	−13.08	2007–2009
AU-Cpr	Calperum	140.59	−34.00	2010–2013
AU-Cum	Cumberland Plain	150.72	−33.61	2012–2013
AU-DaP	Daly River Savanna	131.32	−14.06	2008–2013
AU-DaS	Daly River Cleared	131.39	−14.16	2008–2013
AU-Dry	Dry River	132.37	−15.26	2008–2013
AU-Emr	Emerald, Queensland, Australia	148.47	−23.86	2011–2013
AU-Fog	Fogg Dam	131.31	−12.55	2006–2008
AU-GWW	Great Western Woodlands, Western Australia, Australia	120.65	−30.19	2013–2014
AU-RDF	Red Dirt Melon Farm, Northern Territory	132.48	−14.56	2011–2013
AU-Rig	Riggs Creek	145.58	−36.65	2011–2013
AU-Rob	Robson Creek, Queensland, Australia	145.63	−17.12	2014
AU-Tum	Tumbarumba	148.15	−35.66	2001–2013
AU-Whr	Whroo	145.03	−36.67	2011–2013
BE-Bra	Brasschaat	4.52	51.31	2004–2013
BE-Lon	Lonzee	4.75	50.55	2004–2014
BE-Vie	Vielsalm	6.00	50.31	1996–2014
BR-Sa3	Santarem-Km83-Logged Forest	−54.97	−3.02	2000–2004
CA-NS1	UCI-1850 burn site	−98.48	55.88	2001–2005
CA-NS3	UCI-1964 burn site	−98.38	55.91	2001–2005
CA-NS4	UCI-1964 burn site wet	−98.38	55.91	2002–2005
CA-NS5	UCI-1981 burn site	−98.49	55.86	2002–2005
CA-NS6	UCI-1989 burn site	−98.96	55.92	2001–2005
CA-NS7	UCI-1998 burn site	−99.95	56.64	2002–2005
CA-Qfo	Quebec – Eastern Boreal, Mature Black Spruce	−74.34	49.69	2003–2010
CA-SF1	Saskatchewan – Western Boreal, forest burned in 1977	−105.82	54.49	2003–2006
CA-SF2	Saskatchewan – Western Boreal, forest burned in 1989	−105.88	54.25	2001–2005
CA-SF3	Saskatchewan – Western Boreal, forest burned in 1998	−106.01	54.09	2001–2006
CH-Cha	Chamau	8.41	47.21	2006–2012
CH-Fru	Früebüel	8.54	47.12	2006–2012
CH-Oe1	Oensingen grassland	7.73	47.29	2002–2008
CN-Cha	Changbaishan	128.10	42.40	2004–2005
CN-Cng	Changling	123.51	44.59	2007–2010
CN-Dan	Dangxiong	91.07	30.50	2004–2005
CN-Din	Dinghushan	112.54	23.17	2003–2005
CN-Du2	Duolun_grassland (D01)	116.28	42.05	2006–2008
CN-Ha2	Haibei Shrubland	101.33	37.61	2003–2005
CN-HaM	Haibei Alpine Tibet site	101.18	37.37	2002–2004
CN-Qia	Qianyanzhou	115.06	26.74	2003–2005
CN-Sw2	Siziwang Grazed (SZWG)	111.90	41.79	2010–2012
CZ-BK1	Bily Kriz forest	18.54	49.50	2004–2008
CZ-BK2	Bily Kriz grassland	18.54	49.49	2004–2006
DE-Akn	Anklam	13.68	53.87	2009–2014
DE-Gri	Grillenburg	13.51	50.95	2004–2014
DE-Hai	Hainich	10.45	51.08	2000–2012
DE-Kli	Klingenberg	13.52	50.89	2004–2014
DE-Lkb	Lackenberg	13.30	49.10	2009–2013
DE-Obe	Oberbärenburg	13.72	50.78	2008–2014
DE-RuS	Selhausen Juelich	6.45	50.87	2011–2014
DE-Spw	Spreewald	14.03	51.89	2010–2014
DE-Tha	Tharandt	13.57	50.96	1996–2014

Table B1. Continued.

FLUXNET ID	Name	Long [° E]	Lat [° N]	Years used
DK-NuF	Nuuk Fen	−51.39	64.13	2008–2014
DK-Sor	Soroe	11.64	55.49	1996–2012
ES-LgS	Laguna Seca	−2.97	37.10	2007–2009
ES-Ln2	Lanjaron-Salvage logging	−3.48	36.97	2009
FI-Hyy	Hyytiala	24.30	61.85	1996–2014
FI-Jok	Jokioinen	23.51	60.90	2000–2003
FR-Gri	Grignon	1.95	48.84	2004–2013
FR-Pue	Puechabon	3.60	43.74	2000–2013
GF-Guy	Guyaflux (French Guiana)	−52.92	5.28	2004–2012
IT-CA1	Castel d'Asso1	12.03	42.38	2011–2013
IT-CA2	Castel d'Asso2	12.03	42.38	2011–2013
IT-CA3	Castel d'Asso3	12.02	42.38	2011–2013
IT-Cp2	Castelporziano 2	12.36	41.70	2012–2013
IT-Isp	Ispra ABC-IS	8.63	45.81	2013–2014
IT-Lav	Lavarone	11.28	45.96	2003–2012
IT-Noe	Arca di Noe – Le Prigionette	8.15	40.61	2004–2012
IT-PT1	Parco Ticino forest	9.06	45.20	2002–2004
IT-Ren	Renon	11.43	46.59	1998–2013
IT-Ro1	Roccarespampani 1	11.93	42.41	2000–2008
IT-Ro2	Roccarespampani 2	11.92	42.39	2003–2012
IT-SR2	San Rossore 2	10.29	43.73	2013–2014
IT-SRo	San Rossore	10.28	43.73	1999–2012
IT-Tor	Torgnon	7.58	45.84	2008–2013
JP-MBF	Moshiri Birch Forest Site	142.32	44.39	2003–2005
JP-SMF	Seto Mixed Forest Site	137.08	35.26	2002–2006
NL-Hor	Horstermeer	5.07	52.24	2004–2011
NL-Loo	Loobos	5.74	52.17	1996–2013
NO-Adv	Adventdalen	15.92	78.19	2012–2014
RU-Che	Cherski	161.34	68.61	2002–2005
RU-Cok	Chokurdakh	147.49	70.83	2003–2013
RU-Fyo	Fyodorovskoye	32.92	56.46	1998–2013
RU-Ha1	Hakasia steppe	90.00	54.73	2002–2004
SD-Dem	Demokeya	30.48	13.28	2005–2009
US-AR1	ARM USDA UNL OSU Woodward Switchgrass 1	−99.42	36.43	2009–2012
US-AR2	ARM USDA UNL OSU Woodward Switchgrass 2	−99.60	36.64	2009–2012
US-ARM	ARM Southern Great Plains site- Lamont	−97.49	36.61	2003–2012
US-Blo	Blodgett Forest	−120.63	38.90	1997–2007
US-Ha1	Harvard Forest EMS Tower (HFR 1)	−72.17	42.54	1991–2012
US-Los	Lost Creek	−89.98	46.08	2000–2014
US-MMS	Morgan Monroe State Forest	−86.41	39.32	1999–2014
US-Me6	Metolius Young Pine Burn	−121.61	44.32	2010–2012
US-Myb	Mayberry Wetland	−121.77	38.05	2011–2014
US-Ne1	Mead – irrigated continuous maize site	−96.48	41.17	2001–2013
US-Ne2	Mead – irrigated maize-soybean rotation site	−96.47	41.16	2001–2013
US-Ne3	Mead – rainfed maize-soybean rotation site	−96.44	41.18	2001–2013
US-SRM	Santa Rita Mesquite	−110.87	31.82	2004–2014
US-Syv	Sylvania Wilderness Area	−89.35	46.24	2001–2014
US-Ton	Tonzi Ranch	−120.97	38.43	2001–2014
US-Tw3	Twitchell Alfalfa	−121.65	38.12	2013–2014
US-UMd	UMBS Disturbance	−84.70	45.56	2007–2014
US-Var	Vaira Ranch- Ione	−120.95	38.41	2000–2014
US-WCr	Willow Creek	−90.08	45.81	1999–2014
US-Whs	Walnut Gulch Lucky Hills Shrub	−110.05	31.74	2007–2014
US-Wkg	Walnut Gulch Kendall Grasslands	−109.94	31.74	2004–2014
ZM-Mon	Mongu	23.25	−15.44	2007–2009

Author contributions. BW curated the dataset, carried out the analysis, and drafted the manuscript with inputs from all authors. IT, MF, and WAD created and designed the model. IT provided the model implementation and contributed to data preparation. LM, RMZ, and RvdS produced the VODCA data. StS provided the TRENDY-v7 ensemble data. All authors contributed to discussions about the methods and results and provided feedback and input for the paper.

Competing interests. The contact author has declared that neither they nor their co-authors have any competing interests.

Disclaimer. Publisher's note: Copernicus Publications remains neutral with regard to jurisdictional claims in published maps and institutional affiliations.

Acknowledgements. Benjamin Wild, Ruxandra-Maria Zotta, and Leander Moesinger are supported through the EOWAVE project funded by the TU Wien Wissenschaftspreis 2015, which was awarded to Wouter Dorigo https://climers.geo.tuwien.ac.at/climers/research/vegetation/eowave/ (last access: 25 February 2022). This work used eddy-covariance data acquired and shared by the FLUXNET community, including the following networks: AmeriFlux, AfriFlux, AsiaFlux, CarboAfrica, CarboEurope IP, CarboItaly, CarboMont, ChinaFLUX, Fluxnet-Canada, GreenGrass, ICOS, KoFlux, LBA, NECC, OzFlux-TERN, TCOS Siberia, and USCCC. The FLUXNET eddy-covariance data processing and harmonization was carried out by the ICOS Ecosystem Thematic Centre, AmeriFlux Management Project, and Fluxdata project of FLUXNET, with the support of CDIAC and the OzFlux, ChinaFLUX, and AsiaFlux offices.

Financial support. This research has been supported by the Technische Universität Wien (Wissenschaftspreis 2015 awarded to Wouter Dorigo).

Review statement. This paper was edited by Bo Zheng and reviewed by three anonymous referees.

References

Alemohammad, S. H., Fang, B., Konings, A. G., Aires, F., Green, J. K., Kolassa, J., Miralles, D., Prigent, C., and Gentine, P.: Water, Energy, and Carbon with Artificial Neural Networks (WECANN): a statistically based estimate of global surface turbulent fluxes and gross primary productivity using solar-induced fluorescence, Biogeosciences, 14, 4101–4124, https://doi.org/10.5194/bg-14-4101-2017, 2017.

Anav, A., Friedlingstein, P., Beer, C., Ciais, P., Harper, A., Jones, C., Murray-Tortarolo, G., Papale, D., Parazoo, N. C., Peylin, P., Piao, S., Sitch, S., Viovy, N., Wiltshire, A., and Zhao, M.: Spatiotemporal patterns of terrestrial gross primary production: A review, Rev. Geophys., 53, 785–818, https://doi.org/10.1002/2015RG000483, 2015.

Atkin, O. and Tjoelker, M.: Thermal acclimation and the dynamic response of plant respiration to temperature, Trends Plant Sci., 8, 343–351, https://doi.org/10.1016/S1360-1385(03)00136-5, 2003.

Atkin, O. K., Bruhn, D., Hurry, V. M., and Tjoelker, M. G.: The hot and the cold: unravelling the variable response of plant respiration to temperature, Funct. Plant Biol., 32, 87–105, 2005.

Baldocchi, D., Ryu, Y., and Keenan, T.: Terrestrial Carbon Cycle Variability, F1000 Research, 5, 2371, https://doi.org/10.12688/f1000research.8962.1, 2016.

Baldocchi, D. D.: Assessing the eddy covariance technique for evaluating carbon dioxide exchange rates of ecosystems: past, present and future, Glob. Change Biol., 9, 479–492, https://doi.org/10.1046/j.1365-2486.2003.00629.x, 2003.

Beer, C., Reichstein, M., Tomelleri, E., Ciais, P., Jung, M., Carvalhais, N., Roedenbeck, C., Arain, M. A., Baldocchi, D., Bonan, G. B., Bondeau, A., Cescatti, A., Lasslop, G., Lindroth, A., Lomas, M., Luyssaert, S., Margolis, H., Oleson, K. W., Roupsard, O., Veenendaal, E., Viovy, N., Williams, C., Woodward, F. I., and Papale, D.: Terrestrial gross carbon dioxide uptake: global distribution and covariation with climate, Science, 329, 834–838, https://doi.org/10.1126/science.1184984, 2010.

Bonan, G.: Ecological climatology: Concepts and applications, 2 edn., Cambridge University Press, Cambridge, UK, New York, 550 pp., ISBN 9780521693196, 2008.

Bousquet, E., Mialon, A., Rodriguez-Fernandez, N., Prigent, C., Wagner, F. H., and Kerr, Y. H.: Influence of surface water variations on VOD and biomass estimates from passive microwave sensors. Remote Sens. Environ., 257, 112345, https://doi.org/10.1016/j.rse.2021.112345, 2021.

Bureau of Meteorology: Annual Climate Report, http://www.bom.gov.au/climate/annual_sum/2002/index.shtml (last access: 10 May 2021), 2002.

Bureau of Meteorology: Annual Climate Report, http://www.bom.gov.au/climate/annual_sum/2003/index.shtml (last access: 10 May 2021), 2003.

Bureau of Meteorology: Annual Climate Report, http://www.bom.gov.au/climate/annual_sum/2005/index.shtml (last access: 10 May 2021), 2005.

Campbell, J. E., Berry, J. A., Seibt, U., Smith, S. J., Montzka, S. A., Launois, T., Belviso, S., Bopp, L., and Laine, M.: Large historical growth in global terrestrial gross primary production, Nature, 544, 84–87, https://doi.org/10.1038/nature22030, 2017.

Cox, P. M., Betts, R. A., Jones, C. D., Spall, S. A., and Totterdell, I. J.: Acceleration of global warming due to carbon-cycle feedbacks in a coupled climate model, Nature, 408, 184–187, https://doi.org/10.1038/35041539, 2000.

de Almeida, C. T., Delgado, R. C., Galvao, L. S., de Oliveira Cruz e Aragao, L. E., and Concepcion Ramos, M.: Improvements of the MODIS Gross Primary Productivity model based on a comprehensive uncertainty assessment over the Brazilian Amazonia, ISPRS J. Photogramm., 145, 268–283, https://doi.org/10.1016/j.isprsjprs.2018.07.016, 2018.

De Nijs, A. H. A., Parinussa, R. M., de Jeu, R. A. M., Schellekens, J., and Holmes, T. R. H.: A Methodology to Determine Radio-Frequency Interference in AMSR2

Observations, IEEE T. Geosci. Remote, 53, 5148–5159, https://doi.org/10.1109/TGRS.2015.2417653, 2015.

Drake, J. E., Tjoelker, M. G., Aspinwall, M. J., Reich, P. B., Barton, C. V., Medlyn, B. E., and Duursma, R. A.: Does physiological acclimation to climate warming stabilize the ratio of canopy respiration to photosynthesis?, New Phytol., 211, 850–863, https://doi.org/10.1111/nph.13978, 2016.

Frappart, F., Wigneron, J.-P., Li, X., Liu, X., Al-Yaari, A., Fan, L., Wang, M., Moisy, C., Le Masson, E., Lafkih, Z. A., Vallé, C., Ygorra, B., and Baghdadi, N.: Global Monitoring of the Vegetation Dynamics from the Vegetation Optical Depth (VOD): A Review, Remote Sens., 12, 2915, https://doi.org/10.3390/rs12182915, 2020.

Friedlingstein, P., O'Sullivan, M., Jones, M. W., Andrew, R. M., Hauck, J., Olsen, A., Peters, G. P., Peters, W., Pongratz, J., Sitch, S., Le Quéré, C., Canadell, J. G., Ciais, P., Jackson, R. B., Alin, S., Aragão, L. E. O. C., Arneth, A., Arora, V., Bates, N. R., Becker, M., Benoit-Cattin, A., Bittig, H. C., Bopp, L., Bultan, S., Chandra, N., Chevallier, F., Chini, L. P., Evans, W., Florentie, L., Forster, P. M., Gasser, T., Gehlen, M., Gilfillan, D., Gkritzalis, T., Gregor, L., Gruber, N., Harris, I., Hartung, K., Haverd, V., Houghton, R. A., Ilyina, T., Jain, A. K., Joetzjer, E., Kadono, K., Kato, E., Kitidis, V., Korsbakken, J. I., Landschützer, P., Lefèvre, N., Lenton, A., Lienert, S., Liu, Z., Lombardozzi, D., Marland, G., Metzl, N., Munro, D. R., Nabel, J. E. M. S., Nakaoka, S.-I., Niwa, Y., O'Brien, K., Ono, T., Palmer, P. I., Pierrot, D., Poulter, B., Resplandy, L., Robertson, E., Rödenbeck, C., Schwinger, J., Séférian, R., Skjelvan, I., Smith, A. J. P., Sutton, A. J., Tanhua, T., Tans, P. P., Tian, H., Tilbrook, B., van der Werf, G., Vuichard, N., Walker, A. P., Wanninkhof, R., Watson, A. J., Willis, D., Wiltshire, A. J., Yuan, W., Yue, X., and Zaehle, S.: Global Carbon Budget 2020, Earth Syst. Sci. Data, 12, 3269–3340, https://doi.org/10.5194/essd-12-3269-2020, 2020.

Gilabert, M. A., Sánchez-Ruiz, S., and Moreno, Á.: Annual gross primary production from vegetation indices: A theoretically sound approach, Remote Sens., 9, 193, https://doi.org/10.3390/rs9030193, 2017.

Guisan, A., Edwards, T. C., and Hastie, T.: Generalized linear and generalized additive models in studies of species distributions: setting the scene, Ecol. Model., 157, 89–100, https://doi.org/10.1016/S0304-3800(02)00204-1, 2002.

Hastie, T. and Tibshirani, R.: Generalized Additive Models, vol. 43. CRC press, ISBN 9780412343902, 1990.

Haverd, V., Smith, B., Canadell, J. G., Cuntz, M., Mikaloff-Fletcher, S., Farquhar, G., Woodgate, W., Briggs, P. R., and Trudinger, C. M.: Higher than expected CO_2 fertilization inferred from leaf to global observations, Glob. Change Biol., 26, 2390–2402, https://doi.org/10.1111/gcb.14950, 2020.

Holmes, T. R. H., De Jeu, R. A. M., Owe, M., and Dolman, A. J.: Land surface temperature from Ka band (37 GHz) passive microwave observations, J. Geophys. Res.-Atmos., 114, D04113, https://doi.org/10.1029/2008JD010257, 2009.

Horridge, M., Madden, J., and Wittwer, G.: The impact of the 2002–2003 drought on Australia, J. Policy Model., 3, 285–308, https://doi.org/10.1016/j.jpolmod.2005.01.008, 2005.

Jackson, T. and Schmugge, T.: Vegetation effects on the microwave emission of soils, Remote Sens. Environ., 36, 203–212, https://doi.org/10.1016/0034-4257(91)90057-D, 1991.

Jung, M., Schwalm, C., Migliavacca, M., Walther, S., Camps-Valls, G., Koirala, S., Anthoni, P., Besnard, S., Bodesheim, P., Carvalhais, N., Chevallier, F., Gans, F., Goll, D. S., Haverd, V., Köhler, P., Ichii, K., Jain, A. K., Liu, J., Lombardozzi, D., Nabel, J. E. M. S., Nelson, J. A., O'Sullivan, M., Pallandt, M., Papale, D., Peters, W., Pongratz, J., Rödenbeck, C., Sitch, S., Tramontana, G., Walker, A., Weber, U., and Reichstein, M.: Scaling carbon fluxes from eddy covariance sites to globe: synthesis and evaluation of the FLUXCOM approach, Biogeosciences, 17, 1343–1365, https://doi.org/10.5194/bg-17-1343-2020, 2020.

Le Quéré, C., Andrew, R. M., Friedlingstein, P., Sitch, S., Hauck, J., Pongratz, J., Pickers, P. A., Korsbakken, J. I., Peters, G. P., Canadell, J. G., Arneth, A., Arora, V. K., Barbero, L., Bastos, A., Bopp, L., Chevallier, F., Chini, L. P., Ciais, P., Doney, S. C., Gkritzalis, T., Goll, D. S., Harris, I., Haverd, V., Hoffman, F. M., Hoppema, M., Houghton, R. A., Hurtt, G., Ilyina, T., Jain, A. K., Johannessen, T., Jones, C. D., Kato, E., Keeling, R. F., Goldewijk, K. K., Landschützer, P., Lefèvre, N., Lienert, S., Liu, Z., Lombardozzi, D., Metzl, N., Munro, D. R., Nabel, J. E. M. S., Nakaoka, S., Neill, C., Olsen, A., Ono, T., Patra, P., Peregon, A., Peters, W., Peylin, P., Pfeil, B., Pierrot, D., Poulter, B., Rehder, G., Resplandy, L., Robertson, E., Rocher, M., Rödenbeck, C., Schuster, U., Schwinger, J., Séférian, R., Skjelvan, I., Steinhoff, T., Sutton, A., Tans, P. P., Tian, H., Tilbrook, B., Tubiello, F. N., van der Laan-Luijkx, I. T., van der Werf, G. R., Viovy, N., Walker, A. P., Wiltshire, A. J., Wright, R., Zaehle, S., and Zheng, B.: Global Carbon Budget 2018, Earth Syst. Sci. Data, 10, 2141–2194, https://doi.org/10.5194/essd-10-2141-2018, 2018.

Li, X., Wigneron, J.-P., Frappart, F., Fan, L., Ciais, P., Fensholt, R., Entekhabi, D., Brandt, M., Konings, A. G., Liu, X., Wang, M., Al-Yaari, A., and Moisy, C.: Global-scale assessment and intercomparison of recently developed/reprocessed microwave satellite vegetation optical depth products, Remote Sens. Environ., 253, 112208, https://doi.org/10.1016/j.rse.2020.112208, 2021.

Liu, Y. Y., Van Dijk, A. I., De Jeu, R. A., Canadell, J. G., McCabe, M. F., Evans, J. P., and Wang, G.: Recent reversal in loss of global terrestrial biomass, Nat. Clim. Change, 5, 470–474, https://doi.org/10.1038/nclimate2581, 2015.

Malhi, Y., Rowland, L., Aragao, L. E. O. C., and Fisher, R. A.: New insights into the variability of the tropical land carbon cycle from the El Niño of 2015/2016, Philos. T. R. Soc. B, 373, 20170298, https://doi.org/10.1098/rstb.2017.0298, 2018.

Meesters, A., DeJeu, R., and Owe, M.: Analytical Derivation of the Vegetation Optical Depth From the Microwave Polarization Difference Index, IEEE Geosci. Remote S., 2, 121–123, https://doi.org/10.1109/LGRS.2005.843983, 2005.

Mo, T., Choudhury, B. J., Schmugge, T. J., Wang, J. R., and Jackson, T. J.: A model for microwave emission from vegetation-covered fields, J. Geophys. Res., 87, 11229, https://doi.org/10.1029/JC087iC13p11229, 1982.

Moesinger, L., Dorigo, W., de Jeu, R., van der Schalie, R., Scanlon, T., Teubner, I., and Forkel, M.: The global long-term microwave Vegetation Optical Depth Climate Archive (VODCA), Earth Syst. Sci. Data, 12, 177–196, https://doi.org/10.5194/essd-12-177-2020, 2020.

Monteith, J. L.: Solar radiation and productivity in tropical ecosystems, J. Appl. Ecol., 9, 747–766, https://doi.org/10.2307/2401901, 1972.

Muñoz-Sabater, J., Dutra, E., Agustí-Panareda, A., Albergel, C., Arduini, G., Balsamo, G., Boussetta, S., Choulga, M., Harrigan, S., Hersbach, H., Martens, B., Miralles, D. G., Piles, M., Rodríguez-Fernández, N. J., Zsoter, E., Buontempo, C., and Thépaut, J.-N.: ERA5-Land: a state-of-the-art global reanalysis dataset for land applications, Earth Syst. Sci. Data, 13, 4349–4383, https://doi.org/10.5194/essd-13-4349-2021, 2021.

Nemani, R. R., Keeling, C. D., Hashimoto, H., Jolly, W. M., Piper, S. C., Tucker, C. J., Myneni, R. B., and Running, S. W.: Climate-driven increases in global terrestrial net primary production from 1982 to 1999, Science, 300, 1560–1563, https://doi.org/10.1126/science.1082750, 2003.

O'Sullivan, M., Smith, W. K., Sitch, S., Friedlingstein, P., Arora, V. K., Haverd, V., Jain, A., Kato, E., Kautz, M., Lombardozzi, D., Nabel, J., Tian, H., Vuichard, N., Wiltshire, A., Zhu, D., and Buermann, W.: Climate-driven variability and trends in plant productivity over recent decades based on three global products, Global Biogeochem. Cy., 34, e2020GB006613, https://doi.org/10.1029/2020GB006613, 2020.

Owe, M., de Jeu, R., and Holmes, T.: Multisensor historical climatology of satellite-derived global land surface moisture, J. Geophys. Res., 113, F01002, https://doi.org/10.1029/2007JF000769, 2008.

Pastorello, G., Trotta, C., Canfora, E., et al.: The FLUXNET2015 dataset and the ONEFlux processing pipeline for eddy covariance data, Sci. Data, 7, 225, https://doi.org/10.1038/s41597-020-0534-3, 2020.

Piao, S., Wang, X., Park, T., Chen, C., Lian, X., He, H., Bjerke, J., Chen, A., Ciais, P., Tømmervik, H., Nemani, R., and Myneni, R.: Characteristics, drivers and feedbacks of global greening, Nat. Rev. Earth Environ., 1, 14–27, https://doi.org/10.1038/s43017-019-0001-x, 2019.

Piles, M., Camps-Valls, G., Chaparro, D., Entekhabi, D., Konings, A. G., and Jagdhuber, T.: Remote sensing of vegetation dynamics in agro-ecosystems using smap vegetation optical depth and optical vegetation indices, Int. Geosci. Remote Se., 4346–4349, https://doi.org/10.1109/IGARSS.2017.8127964, 2017.

Rodríguez-Fernández, N. J., Mialon, A., Mermoz, S., Bouvet, A., Richaume, P., Al Bitar, A., Al-Yaari, A., Brandt, M., Kaminski, T., Le Toan, T., Kerr, Y. H., and Wigneron, J.-P.: An evaluation of SMOS L-band vegetation optical depth (L-VOD) data sets: high sensitivity of L-VOD to above-ground biomass in Africa, Biogeosciences, 15, 4627–4645, https://doi.org/10.5194/bg-15-4627-2018, 2018.

Running, S., Mu, Q., and Zhao, M.: MOD17A2H MODIS/terra gross primary productivity 8 d L4 global 500 m SIN grid V006, NASA EOSDIS Land Processes DAAC [data set], https://doi.org/10.5067/MODIS/MOD17A2H.006, 2015.

Running, S. W., Nemani, R., Glassy, J. M., and Thornton, P. E.: MODIS daily photosynthesis (PSN) and annual net primary production (NPP) product (MOD17) Algorithm Theoretical Basis Document, University of Montana, SCF At-Launch Algorithm ATBD Documents, https://www.ntsg.umt.edu/files/modis/ATBD_MOD17_v21.pdf (last access: 25 February 2022), 1999.

Ryan, M. G., Lavigne, M. B., and Gower, S. T.: Annual carbon cost of autotrophic respiration in boreal forest ecosystems in relation to species and climate, J. Geophys. Res.-Atmos., 102, 28871–28883, https://doi.org/10.1029/97JD01236, 1997.

Sade, N., Gebremedhin, A., and Moshelion, M.: Risk-taking plants: Anisohydric behavior as a stress-resistance trait, Plant Signal. Behav., 7, 767–770, https://doi.org/10.4161/psb.20505, 2012.

Schimel, D., Stephens, B. B., and Fisher, J. B.: Effect of increasing CO_2 on the terrestrial carbon cycle, P. Natl. Acad. Sci. USA, 112, 436–441, https://doi.org/10.1073/pnas.1407302112, 2015.

Sen, P. K.: Estimates of the regression coefficient based on Kendall's tau, J. Am. Stat., 63, 1379–1389, 1968.

Servén, D. and Brummitt, C.: pyGAM: generalized additive models in python, Zenodo [code], https://doi.org/10.5281/zenodo.1208723, 2018.

Sitch, S., Friedlingstein, P., Gruber, N., Jones, S. D., Murray-Tortarolo, G., Ahlström, A., Doney, S. C., Graven, H., Heinze, C., Huntingford, C., Levis, S., Levy, P. E., Lomas, M., Poulter, B., Viovy, N., Zaehle, S., Zeng, N., Arneth, A., Bonan, G., Bopp, L., Canadell, J. G., Chevallier, F., Ciais, P., Ellis, R., Gloor, M., Peylin, P., Piao, S. L., Le Quéré, C., Smith, B., Zhu, Z., and Myneni, R.: Recent trends and drivers of regional sources and sinks of carbon dioxide, Biogeosciences, 12, 653–679, https://doi.org/10.5194/bg-12-653-2015, 2015.

Taschetto, A. S. and England, M. H.: El Niño Modoki impacts on Australian rainfall, J. Climate, 22, 3167–3174, https://doi.org/10.1175/2008JCLI2589.1, 2009.

Teubner, I. E., Forkel, M., Jung, M., Liu, Y. Y., Miralles, D. G., Parinussa, R., van der Schalie, R., Vreugdenhil, M., Schwalm, C. R., Tramontana, G., Camps-Valls, G., and Dorigo, W. A.: Assessing the relationship between microwave vegetation optical depth and gross primary production, Int. J. Appl. Earth Obs., 65, 79–91, https://doi.org/10.1016/j.jag.2017.10.006, 2018.

Teubner, I. E., Forkel, M., Camps-Valls, G., Jung, M., Miralles, D. G., Tramontana, G., van der Schalie, R., Vreugdenhil, M., Mösinger, L., and Dorigo, W. A.: A carbon sink-driven approach to estimate gross primary production from microwave satellite observations, Remote Sens. Environ., 229, 100–113, https://doi.org/10.1016/j.rse.2019.04.022, 2019.

Teubner, I. E., Forkel, M., Wild, B., Mösinger, L., and Dorigo, W.: Impact of temperature and water availability on microwave-derived gross primary production, Biogeosciences, 18, 3285–3308, https://doi.org/10.5194/bg-18-3285-2021, 2021.

Theil, H.: A rank-invariant method of linear and polynomial regression analysis, Indagat. Math., 12, 173, 1950.

Tian, F., Brandt, M., Liu, Y. Y., Verger, A., Tagesson, T., Diouf, A. A., Rasmussen, K., Mbow, C., Wang, Y., and Fensholt, R.: Remote sensing of vegetation dynamics in drylands: Evaluating vegetation optical depth (VOD) using AVHRR NDVI and in situ green biomass data over West African Sahel, Remote Sens. Environ., 177, 265–276, https://doi.org/10.1016/j.rse.2016.02.056, 2016.

Tjoelker, M., Oleksyn, J., and Reich, P.: Modelling respiration of vegetation: evidence for a general temperature-dependent Q(10), Glob. Change Biol., 7, 223–230, https://doi.org/10.1046/j.1365-2486.2001.00397.x, 2001.

Tramontana, G., Jung, M., Schwalm, C. R., Ichii, K., Camps-Valls, G., Ráduly, B., Reichstein, M., Arain, M. A., Cescatti, A., Kiely, G., Merbold, L., Serrano-Ortiz, P., Sickert, S., Wolf, S., and Papale, D.: Predicting carbon dioxide and energy fluxes across global FLUXNET sites with regression algorithms, Biogeosciences, 13, 4291–4313, https://doi.org/10.5194/bg-13-4291-2016, 2016.

Turner, D. P., Ritts, W. D., Cohen, W. B., Gower, S. T., Running, S. W., Zhao, M., Costa, M. H., Kirschbaum, A. A., Ham, J. M., Saleska, S. R., and Ahl, D. E.: Evaluation of MODIS NPP andGPP products across multiple biomes, Remote Sens. Environ., 102, 282–292, https://doi.org/10.1016/j.rse.2006.02.017, 2006.

Van der Schalie, R., de Jeu, R., Kerr, Y., Wigneron, J., Rodríguez-Fernández, N., Al-Yaari, A., Parinussa, R., Mecklenburg, S., and Drusch, M.: The merging of radiative transfer based surface soil moisture data from SMOS and AMSR-E, Remote Sens. Environ., 189, 180–193, https://doi.org/10.1016/J.RSE.2016.11.026, 2017.

Vreugdenhil, M., Dorigo, W. A., Wagner, W., De Jeu, R. A., Hahn, S., and Van Marle, M. J.: Analyzing the Vegetation Parameterization in the TU-Wien ASCAT Soil Moisture Retrieval, IEEE T. Geosci. Remote, 54, 3513–3531, https://doi.org/10.1109/TGRS.2016.2519842, 2016.

Walker, A. P., Kauwe, M. G. D., Bastos, A., Belmecheri, S., Georgiou, K., Keeling, R. F., McMahon, S. M., Medlyn, B. E., Moore, D. J. P., Norby, R. J., Zaehle, S., Anderson-Teixeira, K. J., Battipaglia, G., Brienen, R. J. W., Cabugao, K. G., Cailleret, M., Campbell, E., Canadell, J. G., Ciais, P., Craig, M. E., Ellsworth, D. S., Farquhar, G. D., Fatichi, S., Fisher, J. B., Frank, D. C., Graven, H., Gu, L., Haverd, V., Heilman, K., Heimann, M., Hungate, B. A., Iversen, C. M., Joos, F., Jiang, M., Keenan, T. F., Knauer, J., Körner, C., Leshyk, V. O., Leuzinger, S., Liu, Y., MacBean, N., Malhi, Y., McVicar, T. R., Penuelas, J., Pongratz, J., Powell, A. S., Riutta, T., Sabot, M. E. B., Schleucher, J., Sitch, S., Smith, W. K., Sulman, B., Taylor, B., Terrer, C., Torn, M. S., Treseder, K. K., Trugman, A. T., Trumbore, S. E., van Mantgem, P. J., Voelker, S. L., Whelan, M. E., and Zuidema, P. A.: Integrating the Evidence for a Terrestrial Carbon Sink Caused by Increasing Atmospheric CO_2, New Phytol., 229, 2413–2445, https://doi.org/10.1111/nph.16866, 2020.

Wang, L., Zhu, H., Lin, A., Zou, L., Qin, W., and Du, Q.: Evaluation of the Latest MODIS GPP Products across Multiple Biomes Using Global Eddy Covariance Flux Data, Remote Sens., 9, 5, https://doi.org/10.3390/rs9050418, 2017.

Wardle, G. M., Pavey, C. R., and Dickman, C. R.: Greening of arid Australia: new insights from extreme years, Austral. Ecol., 38, 731–740, https://doi.org/10.1111/aec.12073, 2013.

Welp, L. R., Keeling, R. F., Meijer, H. A., Bollenbacher, A. F., Piper, S. C., Yoshimura, K., Francey, R. J., Allison, C. E., and Wahlen, M.: Interannual variability in the oxygen isotopes of atmospheric CO_2 driven by El Niño, Nature, 477, 579–582, https://doi.org/10.1038/nature10421, 2011.

Wilcox, R. R.: Fundamentals of modern statistical methods: substantially improving power and accuracy, Springer, New York, USA, 34–35, https://doi.org/10.1007/978-1-4757-3522-2, 2010.

Wild, B., Teubner, I., Moesinger, L., Zotta, R. M., Forkel, M., Van der Schalie, R., Sitch, S., and Dorigo, W. A.: VODCA2GPP (Version 1.0.0), Technische Universität Wien [data set], https://doi.org/10.48436/1k7aj-bdz35, 2021.

Wythers, K. R., Reich, P. B., and Bradford, J. B.: Incorporating temperature-sensitive Q10 and foliar respiration acclimation algorithms modifies modeled ecosystem responses to global change, J. Geophys. Res.-Biogeo., 118, 77–90, https://doi.org/10.1029/2011JG001897, 2013.

Xiao, J., Chevallier, F., Gomez, C., Guanter, L., Hicke, J. A., Huete, A. R., Ichii, K., Ni, W., Pang, Y., Rahman, A. F., and Sun, G.: Remote sensing of the terrestrial carbon cycle: A review of advances over 50 years, Remote Sens. Environ., 233, 111383, https://doi.org/10.1016/j.rse.2019.111383, 2019.

Xie, X., Li, A., Jin, H., Bian, J., Zhang, Z., and Nan, X.: Comparing Three Remotely Sensed Approaches for Simulating Gross Primary Productivity over Mountainous Watersheds: A Case Study in the Wanglang National Nature Reserve, China, Remote Sens., 13, 3567, https://doi.org/10.3390/rs13183567, 2021.

Zhai, P.-M., Yu, R., Guo, Y.-J., Li, Q.-X., Ren, X.-J., Wang, Y.-Q., Xu, W.-H., Liu, Y.-J., and Ding, Y.-H.: The strong El Niño of 2015/16 and its dominant impacts on global and China's climate, J. Meteorol. Res., 30, 283–297, https://doi.org/10.1007/s13351-016-6101-3, 2016.

Zhang, Y. and Aizhong Y.: Would the obtainable gross primary productivity (GPP) products stand up? A critical assessment of 45 global GPP products, Sci. Total Environ., 783, 146965, https://doi.org/10.1016/j.scitotenv.2021.146965, 2021.

Zhao, M., Heinsch, F. A., Nemani, R. R., and Running, S. W.: Improvements of the MODIS terrestrial gross and net primary production global data set, Remote Sens. Environ., 95, 164–176, https://doi.org/10.1016/j.rse.2004.12.011, 2005.

Zotta, R. M., Moesinger, L., Van der Schalie, R., Vreugdenhill, M., Preimesberger, W., and Dorigo, W. A. (preliminary author list): VODCA v2: An improved multi-sensor and frequency vegetation optical depth dataset for long-term vegetation monitoring (preliminary title), in preparation, 2022.